Journal of the Mechanical Behavior of Biomedical Materials 173 (2026) 107201

Contents lists available at ScienceDirect

Journal of the Mechanical Behavior of Biomedical Materials

journal homepage: www.elsevier.com/locate/jmbbm

Electron beam powder bed fusion additive manufacturing of Ti6Al4V alloy lattice structures: orientation-dependent fatigue strength and crack growth behaviour under compressive cyclic loading

Yawen Huang, Zhan Wen Chen *

Department of Mechanical Engineering, Auckland University of Technology, New Zealand

ARTICLE INFO

Keywords:
Cell orientation
Stress concentration
Crack initiation
Crack growth

ABSTRACT

Sufficiently high fatigue strength is required for lattices made using electron beam powder bed fusion (EBPBF) for hip implants and understanding the anisotropic fatigue behaviour of EBPBF lattices is necessary for implant design. In this work, the combined effects of loading direction (LD) and cell orientation of EBPBF-Ti6Al4V lattices on the fatigue strength of the structures under cyclic compressive loading have been studied. Simple cubic (SC) ([001]//LD, [011]//LD and [111]//LD) lattices with a relative density of 0.36 were EBPBF made, tested and examined. The fatigue strength of [001]//LD lattices has been determined to be ~190 MPa at 5×10^6 cycles, ~8 times higher than that of [011]//LD or [111]//LD lattices. The low fatigue strength of the non-[001]//LD lattices resulted from crack initiation readily occurring in the high tension locations, which are the top and bottom locations of each unit cell. Sideway growth of cracks leading to fracturing along (001) will be shown. This failure mechanism is absent in [001]//LD lattices and thus their fatigue strength is high. Examining the data in the literature has shown that fatigue strength values of all non-SC lattice structures are low, likely due to the same failure mechanism identified for non-[001]//LD SC lattices in this study.

1. Introduction

With powder bed fusion (PBF) metal additive manufacturing (AM) having matured and now being increasingly used in industry, the technology has also been more widely applied for making lattice structures (du Plessis et al., 2022). A possible application of lattice structure PBF is for making orthopedic implants as PBF-Ti6Al4V lattice structures have been shown to potentially match bones biologically and mechanically (Dias et al., 2024). To meet the requirements for mimicking bones, the implants need to be highly porous. It is known that pore sizes in implants should range from 0.3 to 0.6 mm for osseointegration and osteoconduction (Barba et al., 2019). The distinctive capability of PBF is the little restriction on part geometries and the making of porous implants has thus been viewed as the best example of utilising PBF-AM (Foti et al., 2023). This is because making the highly porous and small pore-size structures are beyond the capabilities of most other manufacturing technologies. Laser PBF (LPBF) and electron beam PBF (EBPBF) with the beam size down to 40 μm (Khorasani et al., 2020) and 200 μm (Fu and Körner, 2022), respectively, are highly suitable for producing lattice or cellular structures for implant applications. This suitability is well accepted (Sing et al., 2016; Barba et al., 2019; Hanks et al., 2020; Benedetti et al., 2021; Korkmaz et al., 2022; Dias et al., 2024).

However, for potentially applying PBF to produce high-quality orthopaedic hip implants, the strength under cyclic loading needs to be sufficient. This is because a hip implant needs to support the load of an upper body cyclically in everyday life and the required fatigue life of the implant clearly needs to be sufficiently high. It is clear that, for hip implant application, the high-cycle fatigue strength of porous structures is a major concern and the fatigue behaviour of PBF lattice structures needs to be deeply studied (Dias et al., 2024; 19 Guo et al., 2022). The recent review (Dias et al., 2024) has shown that there has only been one fatigue study of a PBF femoral stem containing a portion of lattice structure. Knowledge based on which lattice structures are designed for cyclic loading, as is required for designing porous femoral stem, appears to be insufficient at present. Ren et al. (2019) and Benedetti et al. (2021) conducted reviews on fatigue behaviour and properties of porous structures additively manufactured. The reviews have shown that only a limited number of studies were conducted before 2021 and insufficient data of compression-compression fatigue is available, on which the design of porous stems would need to be based. As illustrated in the case

* Corresponding author.
E-mail address: zhan.chen@aut.ac.nz (Z.W. Chen).

https://doi.org/10.1016/j.jmbbm.2025.107201
Received 1 May 2025; Received in revised form 30 August 2025; Accepted 12 September 2025
Available online 15 September 2025

studies of femoral stems (Dias et al., 2024), stems are dominantly subjected to compression-compression cyclic loading.

It is thus worthwhile to briefly summarise the findings of the compression-compression fatigue studies of Ti-alloy PBF porous structures, as presented in Table 1. The table contains the values of relative density (ρ_r) meaning the ratio of lattice density to solid density (ρ_L/ρ_S), the run-out cycle number (N_{RO}), the corresponding maximum compressive stress (σ_M) with $R=F_{min}/F_{max} = \sigma_{min}/\sigma_{max} = 10$, and also other information (orientation, as-built, HIP or HT-annealing for LPBF) if the information is available and stated from the various studies. Run-out in a fatigue life test means that the sample does not fail when the test number reaches a pre-set cycle number. All data from EBPBF studies available (since 2011) and from LPBF since 2020 have been included in the table. For a better understanding of these data, σ_M values have been plotted against ρ_r and shown in Fig. 1. In the plot, data of the lattice structures that are not simple cubic (SC) lattice structures have been grouped into one, except for the FCCm and the optimised lattices the data of which have been separately grouped. As listed in Table 1, N_{RO} values range from 1×10^6 to 1×10^7. This needs to be borne in mind when trends of these data are suggested.

Fig. 1 shows that, in general, fatigue strength values of non-SC lattice structures are low. For example, for $\rho_r = 0.4$, $\sigma_M \sim 25$ MPa which can be viewed a low value for the given ρ_r. There are two exceptions. The first is the sample with diamond unit cells and with the [011]//LD orientation, for which, σ_M is high at 80 MPa ($N_{RO} = 1 \times 10^6$) for $\rho_r = 0.25$. For [001]//LD and [111]//LD lattices of the same unit cell and ρ_r (=0.25), σ_M values are low at 13–18 MPa. The considerable difference in σ_M of the [011]//LD sample compared to the other two has been suggested to be due to the geometrical deviation due to manufacturing (Cutolo and Van Hooreweder, 2022). The second is the FCCm (Alaña et al., 2021) and the topologically optimised (Wu et al., 2024) lattice samples. It should be noted that, viewing the drawings of the unit cells from the two studies has suggested the two being the same type of unit cell, FCCm (FCC modified). Thus, FCCm lattice is an exception to the non-SC lattice structures and, as shown in Fig. 1, σ_M has increased to 55 MPa when ρ_r increases to 0.3, for $N_{RO} = 1 \times 10^6$. However, in both studies (Alaña et al., 2021; Wu et al., 2024), how the FCCm lattices compared to other non-SC lattices may be more favourable in support of cyclic loading for longer crack initiation cycles or in having slow rates of crack growth has not been more explicitly explained.

In comparison to non-SC lattice samples, data for SC lattice samples in Fig. 1 are generally higher in fatigue strength, although the data are seen highly scattered and limited. On the other hand, it should also be noted that data for FCCm samples are all based on $N_{RO} = 1 \times 10^6$. Thus, it may be stated that σ_M values of SC lattices ($N = 1 \times 10^7$) are significantly higher than those of FCCm samples, if the FCCm samples were tested for 1×10^7 cycles, as σ_M values should be lowered. It is also noted that, for the three studies using SC lattice samples or including the use of SC samples, the SC samples are all [001]//LD. Furthermore, in these studies, crack initiation and propagation have not been examined in detail and how loading support of SC lattices is more favourable than non-SC lattices and thus having long fatigue life for the same loading is still not well understood.

The review above has suggested that, although compressive fatigue strength values of SC lattices are higher than those of non-SC lattices, the effect of LD with respect to unit cell orientation on fatigue strength has not been studied. This means that the anisotropic fatigue behavior of SC lattices has not been sufficiently understood. For an implant to support loading after implanting, actual compressive loading acting onto the implant can be in different directions and this needs to be considered in implant design. Thus, in this study, the combined effects of LD and the unit cell orientation of SC lattices on the compressive fatigue strength are investigated. For this, Ti6Al4V SC lattice samples were EBPBF built with $\rho_r = 0.36$ and thus $\rho_L = 1.60$ g/cm^3 by design. The ρ_r value is within the range that has shown to be suitable for implant applications (Ziaie et al., 2024). Samples were compressively tested under cyclic loading. Post-test examinations were conducted focusing on the crack initiation locations, through which the limiting factors of fatigue life can be identified. The examination has included samples tested under quasi-static loading to provide a comparison and thus to better understand how cyclic loading affects the failure process. Finite element simulations were performed to aid the understanding of locations where crack initiation can more readily occur. We hypothesize that fatigue strength would decrease if [001] is not parallel to LD. We also hypothesize that the non-[001]//LD orientations may provide unfavorable and localized stress concentration locations for cracks to readily grow, thus decreasing fatigue strength.

2. Experimental procedures

Ti6Al4V lattice samples were built using an Arcam Q10 EBM production machine (Huang et al., 2024). Briefly, the proprietary Arcam

Table 1
Approximate fatigue strength data of Ti6Al4V (except β−Ti alloys) PBF lattice structures from literature with tests conducted using R = 10.

Unit cell	ρ_r	Condition	N_{RO}	σ_M, MPa	Ref.
EBPBF					
Diamond	0.17–0.40	As-built	2.2×10^6	3–23	Hrabe et al. (2011)
Rhombi dodecahedron	0.17–0.38	As-built	1×10^7	1–15	Li et al. (2012)
G7	0.38	As-built	1×10^7	10	Zhao et al. (2016)
Rhombic dodecahedron	0.36	As-built	2×10^6	14	
Simple cubic	0.37	As-built, [001]//LD		115	
Simple cubic	0.28	As-built, HT, [001]//LD	1×10^7	43, 52	Yuan et al. (2018)
Simple cubic	0.3	As-built, [001]//LD	1×10^7	85	Radlof et al. (2021)
LPBF					
Cuboctahedron COH-Z	0.16, 0.50,0.67	As-built	1×10^6	7,44,110	Wu et al. (2020)
		HT		10,54,98	
Diamond	0.37	As-built	1×10^6	25	Karami et al. (2020)
Simple cubic, cubic irregular	0.24,0.29	As-built	1×10^7	102,7	Raghavendra et al. (2021)
Star, star irregular	0.23			24,5	
Cross, cross irregular	0.21,0.20			3,3	
Trabecular	0.29			10	
FCCm	0.1,0.2,0.3	HIP	1×10^6	5,28,55	Alaña et al. (2021)
Gyroid	0.25	As-built	1×10^6	24	Yang et al. (2021)
Gyroid	0.26,0.30	As-built	2×10^6	8	Mahmoud et al. (2021)
Diamond	0.25	AB [001].[011],[111]//LD	5×10^6	13,80,18	Cutolo and Van Hooreweder (2022)
COH	0.31	As-built, HIP	1×10^6	9,20	Wu et al. (2022)
(βTi21S) octet truss	0.26	As-built, HIP	1×10^7	7,17	Jam et al. (2024)
β-Ti Rhom. dodecahedron	0.25	As-built	1×10^6	10	Wu et al. (2024)
Topologically Optimised		HT		50	

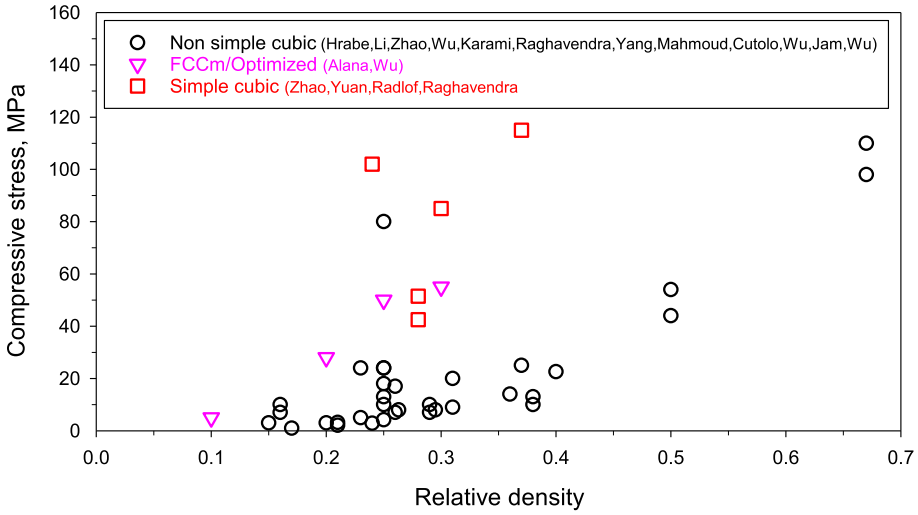

Fig. 1. Fatigue strength data, maximum compression stress (σ_M) at run-out plotted against relative density (ρ_r), from literature as listed in Table 1.

EBPBF parameter control theme used for making lattice/porous structures in industry practice was used in building the samples. The unit cell of all the lattice samples is SC, as rotating an SC lattice structure allows for the orientation of the structure and each strut in the structure to be readily and clearly defined. Three different orientations have been considered and thus, three groups of samples have been built for the effect of cell orientation on compressive fatigue strength of the structures to be studied. For all three groups of samples, the cell size is the same with each of the six cell edges (a_{Cell}) being 1.1 mm and the designed strut size being 0.5 mm, giving the designed value of apparent relative density $\rho_L/\rho_S = 0.36$ ($\rho_L = 1.60$ g/cm^3). The apparent diameter in the design of a lattice sample is 10 mm and the height is 20 mm for the lattice portion. Thus, the ratio of height over diameter is 2, meeting the required ratio specified in ASTM Standard E9-09, 2019. On the top of and below the lattice portion, a solid and larger portion was added/built as support (for compression-fatigue test) and there should be little deformation in these solid portions during testing.

The unit cell and orientation of each group of samples are illustrated in Fig. 2, with build direction parallel to load direction (LD). Two coordinates (x'y'z' the original coordinate and xyz the new coordinate) are shown for each group in Fig. 2. In the first group, the two are the same with [001] (=[001]') parallel to build orientation (=LD) and thus the samples of this orientation are referred to as [001]//LD samples. For the second group, the original unit cell (as in group one) has rotated about [001]' for 45° so that [011]//LD, thus, referred to as [011]//LD samples. For the third group, the original unit cell has rotated about $[1\bar{1}0]$' for 54.7° so that [111]//LD, referred to as [111]//LD samples. Thus, if the fracture direction and plane of a lattice sample are cell orientation dependant, the features of fracture can be more commonly and readily explained for all the samples using the xyz coordinate instead of the x'y'z' coordinate.

As has been explained, a sample consists of a top and a bottom solid portion and a lattice portion in the middle (Fig. 3). A solid portion (either the top or the bottom), by design, can be viewed as a conical frustum plus a circular disk. The two diameters of the frustum faces are 10 mm and 15 mm and the high is 4.5 mm. The diameter of the circular disk is 10 mm and the high 2 mm. It can be shown that the volume of each solid portion is 0.9124 cm^3 (the conical frustum being 0.5589 cm^3 and the circular disk being 0.3535 cm^3). Then, the bottom portion and top solid portion together should be 1.8248 cm^3. Take 4.43 g/cm^3 as the density of Ti6AlV4, the solid portions in a sample weight 8.0839g. Samples have been weighted with 11 samples for each orientation. The values are (mean and standard error) 10.26 ± 0.05g, 10.17 ± 0.05g, and 10.36 ± 0.06g, respectively, for [001]//LD samples, for [011]//LD samples, and for [111]//LD samples. As has been explained, the design/apparent diameter of the lattice portion of a sample is 1 cm and the

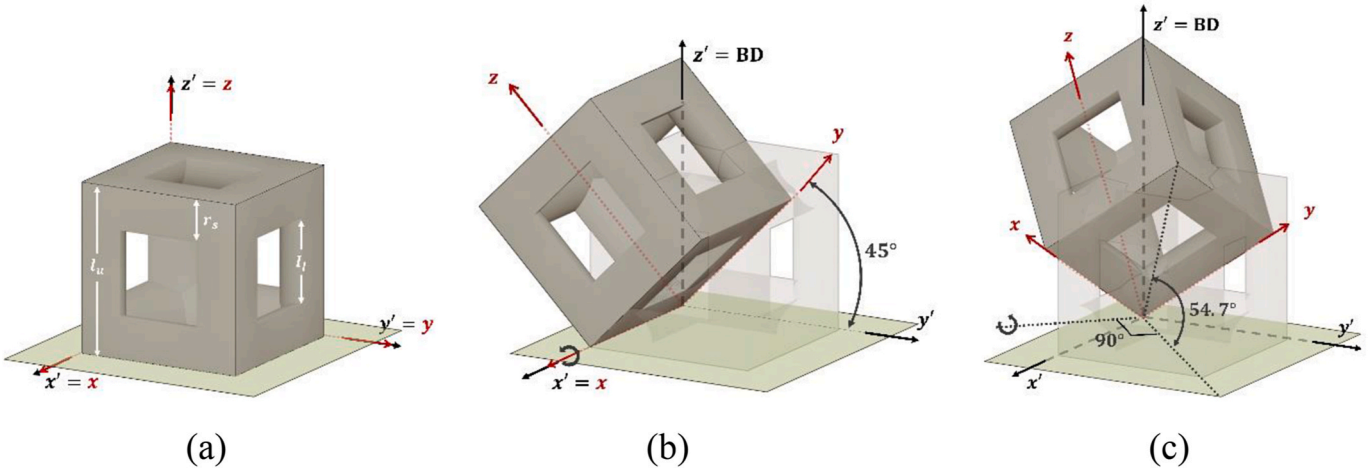

Fig. 2. Illustrations of a simple cubic unit cell orientated in (a) [001]//LD, (b) [011]//LD, and (c) [111]//LD, x'y'z' coordinate and in xyz coordinate. Build direction (BD) is parallel to z' and is indicated.

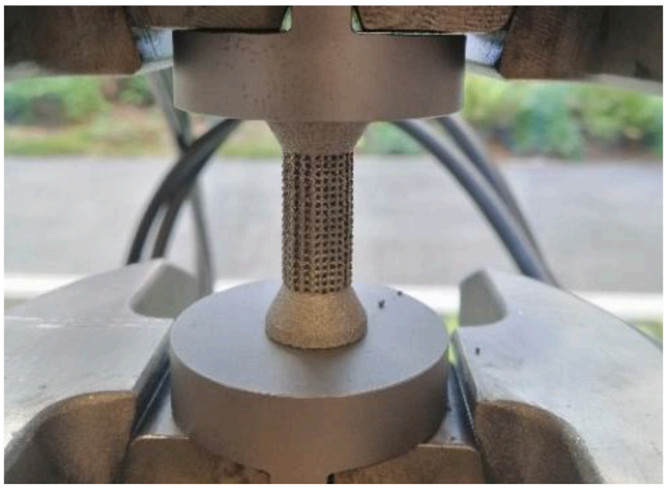

Fig. 3. Photo showing a [001]//LD sample being tested under compression cyclic loading.

height 2 cm, and thus the volume is 1.57 cm^3. If this portion is solid, the weight is 6.955g. Then, the estimated relative density values are: (10.26–8.083)g/6.955g = 0.313 (for [001]//LD samples), (10.17–8.083)g/6.955g = 0.300 (for [011]//LD samples), and (10.36–8.083)g/6.955g = 0.327 for [111]//LD samples.

Fatigue testing was carried out under sinusoidal axial compression with constant loading amplitude in an MTS Landmark servo-hydraulic testing machine. All tests were conducted using the stress ratio R = 10 and the oscillation frequency of 20 Hz. Fig. 3 shows a lattice sample being tested. Typically, before the start of a test, the top press plate gripped is lowered so that the surface of the plate is ~0.5 mm to the top of the sample. When a test starts, the top press plate is lowered slowly (controlled by the machine) to contact the sample and the load then gradually (cycle by cycle) increases. The test will stop when the maximum to minimum peak-to-peak displacement $\Delta d_p(N)$ of the crosshead has increased to a value as expressed in the following equation:

$$\Delta d_P(N) = \Delta d_{p(N=1,000)} + m{\cdot}\Delta d_{p(N=1,000)} = \Delta d_{p(N=1,000)} \times (1+m) \qquad \text{Eq. 1}$$

where $\Delta d_{p(N = 1000)}$ is the maximum to minimum peak-to-peak displacement at 1000 cycles and m is the tolerance percentage of $\Delta d_p(N)$. The fatigue life meaning the cycle number to failure (N) for σ_M is then N. It normally takes a few tens of cycles to reach the required loading and thus cycle 1000 as the reference representing the beginning of the test but the cyclic loading has been stabilised.

After testing and visual examination, the tested samples were examined using a Hitachi SU-70 field emission scanning electron microscope (FE-SEM) to observe where cracks may have initiated and how cracks may have grown. The SEM examination also included using samples that have been sectioned so as to more clearly illustrate the crack paths in the struts inside the lattice structures. The sectioning of each sample was carried out in the way that the sectioned plane was parallel to LD and the fractured plane was normal to the sectioned plane, so that fracture direction can be viewed. The sectioned samples were mounted, ground and polished before being examined under the FE-SEM. Sectioning by wire cutting and grinding/polishing were carefully carried out so that the internal struts in a selected section could be polished but preserved after grinding/polishing for the plane of struts to be examined.

To estimate the stress distribution in the lattices so as to understand the crack initiation sites, 3D finite element (FE) models were developed using ANSYS static solver. The lattices were meshed using SOLID 187 Tetrahedral elements with a mesh size of 0.1 mm after performing a sensitivity analysis. Each FE model consisted of a lattice structure placed between a top and a bottom solid plate. Previous studies suggested that the mechanical properties of the non-stochastic cellular materials could be well predicted by using a low number of unit cells (Mehboob et al., 2018; Kadkhodapour et al., 2015; Peng et al., 2020). Thus, to improve the computational efficiency, 3 × 3 × 3 unit cell lattices were modelled based on the sensitivity analysis of unit cell numbers. As increasing the number of cells from 1 × 1 × 1 to 3 × 3 × 3, the variation in effective Young's modulus and 0.2 % yield stress converged with a tolerance less than 5 %. The bottom plate was constrained in terms of all degrees of freedom, while an axial displacement boundary condition was applied to the top surface of the top plate achieving an engineering strain of 5 % in 20 increments. The contact behaviour between the plates and the lattice was set as bonded. Mechanical property values of bulk Ti6Al4V are: density ρ_S = 4430 kg/m^3, Young's modulus E = 120 GPa, Posson's ratio ν = 0.323 (Ansys® Academic Research Mechanical, 2023). The bi-linear plasticity model was applied, where yield strength was 1,001 MPa and tangent modulus after yielding was 1,332 MPa.

3. Results and discussion

3.1. S-N data and orientation-dependent fatigue strength

It is necessary to first present and inspect the Δd_p-N values/curves. This is because there is a need for these Δd_p-N curves to be referred to when S-N data and fatigue failure are discussed. The curves are shown in Fig. 4. Test curves except those for the run-out samples and the 230 MPa-[001]//LD sample show that, towards the end of each test, an initially more gradual and soon after a rapid but small increase in Δd_p has triggered the stop of the test. The use of m values from 92 % to 150 % does not affect the N values. The 230 MPa-[001]//LD sample is different and the Δd_p values gradually increased and eventually the test was terminated when the more gradual increase in Δd_p reached m = 92 %. For [011]//LD and [111]//LD samples, the rapid increase in Δd_p to trigger the stop of the test is more pronounced. The use of higher values, m= (135 %–150 %), was necessary in some tests so that the samples could fracture more completely and the features of fracturing could be examined.

Fatigue data of the three different cell orientated samples in the form of σ_M (=$|\sigma_{min}|$, thus maximum compression stress) plotted against the cycle number (N) to failure are plotted in Fig. 5, means and 95 % confidence intervals for data of [001]//LD and [011]//LD samples are also included. These curves of means and intervals are based on the regression analysis conducted using SigmaPlot (version 14) that was also used to plot the graph. Fig. 5 shows that, for the non-[001]//LD lattices, the (negative) slope is steep and thus N is strongly dependent on applied stress. For [001]//LD lattices, the dependence is weak. The maximum number of cycles of the fatigue testing without failure, thus taken as run-out, is 5 × 10^6 in the present work. This is based on consideration that, as explained in Introduction, the understanding of the fatigue behaviour of the lattice structures can be potentially applicable for femoral stem implants manufactured using PBF. As specified in the international standard of testing the femoral stem implants, the required cycle number without the failure of the implants is 5 × 10^6 (BS ISO 7206-4, 2016). Also in Fig. 5, in order to evaluate how cyclic loading affects the fatigue strength of the lattice structures, quasi-static ultimate compression strength (σ_{UCS}) data (Huang et al., 2024) are also indicated on the left of the graph.

Fig. 5 shows that, clearly, strength values of [001]//LD lattices are considerably higher than the strength values of both [011]//LD and [111]//LD lattices. Comparative values from data in Fig. 5 are summarised in Table 2. For [001]//LD lattices, σ_M has decreased only 2 % as N increases to 10^4 and has only decreased moderately (17 %) as N increases to 10^6. On the other hand, for both [011]//LD and [111]//LD lattices, σ_M has decreased considerably (56 %) as N increases to 10^4 and has decreased substantially (374 %) as N increases to 10^6. The comparison can also be seen that, the strength ratio $\sigma_{UCS[001]}/\sigma_{UCS[011]}$ (or

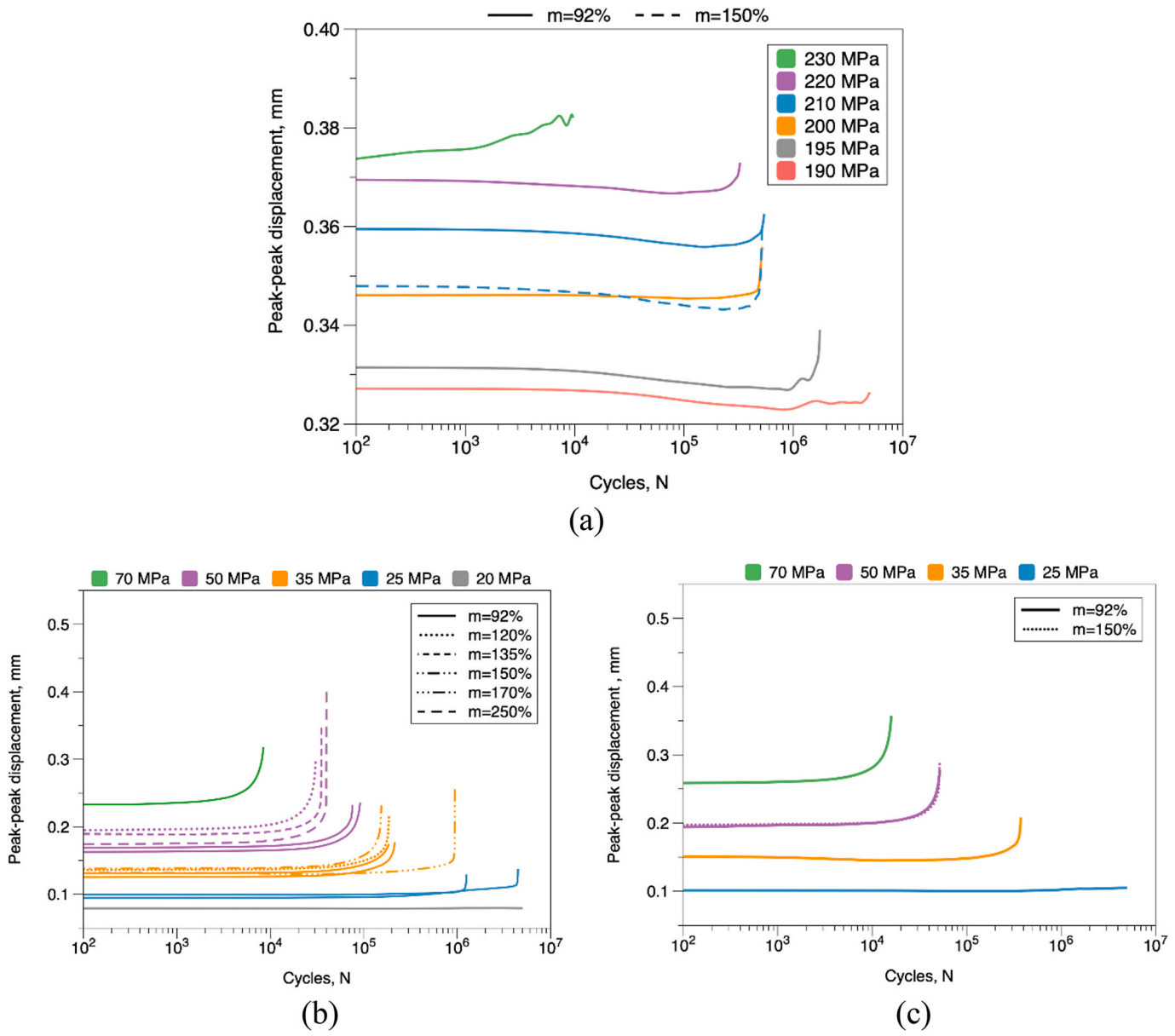

Fig. 4. Representative curves of peak-peak displacement plotted (Δd_p) against cycle number for (a) [001]//LD samples, (b) [011]//LD, and (c) [111]//LD samples. Note: colours represent the stress levels and types of lines represent m values, as indicated in each graph.

$\sigma_{UCS[001]}/\sigma_{UCS[111]}$) is 2.2 but $\sigma_{M[001]}/\sigma_{M[011]}$ (or $\sigma_{M[001]}/\sigma_{M[111]}$) is 3.3 at $N = 10^4$ and 8.7 at $N = 10^6$, as listed in Table 2. This shows that cyclic loading has a significantly more adverse effect on the fatigue strength of the non-[001]//LD lattice samples than that of the [001]//LD samples. In the following sections, the various cell orientation-dependent fracture behaviours are revealed to explain the reasons for the effects of cyclic loading on fatigue strength as just referred to.

3.2. Orientation-dependent fracture directions and planes

In order to evaluate and discuss the orientation effects on fatigue strength, the various directions need to be defined first. As will be shown, in non-[001]/LD samples, they have failed by shear fracturing along a plane. The fracture plane (FP) between the top fractured portion and the bottom fractured portion represented by a top (white) disk and a bottom (yellow) disk, respectively, is drawn in Fig. 6. In the figure, the fracture direction (FD) and LD have also been indicated. Then, there is a specific front view direction (FVD_S) that the fractured sample can be placed so that $\angle FVD_S/LD = 90°$ and also $\angle FVD_S/FD = 90°$. By taking a photograph of a fractured sample from this FVD_S viewing, the shear angle in relation to LD (α meaning ∠FD/LD in Fig. 6) can directly be measured in the image. Knowing α, as the lattice orientation is already known, the equivalent miller index (h, k and l) of FP can be determined.

FD and FP are now first illustrated for quasi-static tested samples before presenting the examination of fatigue-tested samples. As shown in Fig. 7a and b, the untested samples (left samples) have been intentionally placed so that the front view is (100) for both [001]//LD and [011]//LD samples, respectively. A square including an area of four cells in (100) (in yellow) can largely fit the square of four cells of the sample. For the [111]//LD sample (Fig. 7c, left), the aspect ratio (the length of the longer edge over the length of the shorter edge) of (110) in a unit cell is 1.414. The shorter edge of (110) in a unit cell should be at 54.7° to [111] (and the longer edge 35.3°). Fig. 7c (left) shows that if the original yellow square (as in the [001]//LD sample) is stretched 1.414 times in the vertical direction and rotates for 35.3° clockwise, it fits the cells closely. Note a photograph only represents the dimensions of the object approximately.

For the [001]//LD samples (Fig. 7a), the second to the right sample is

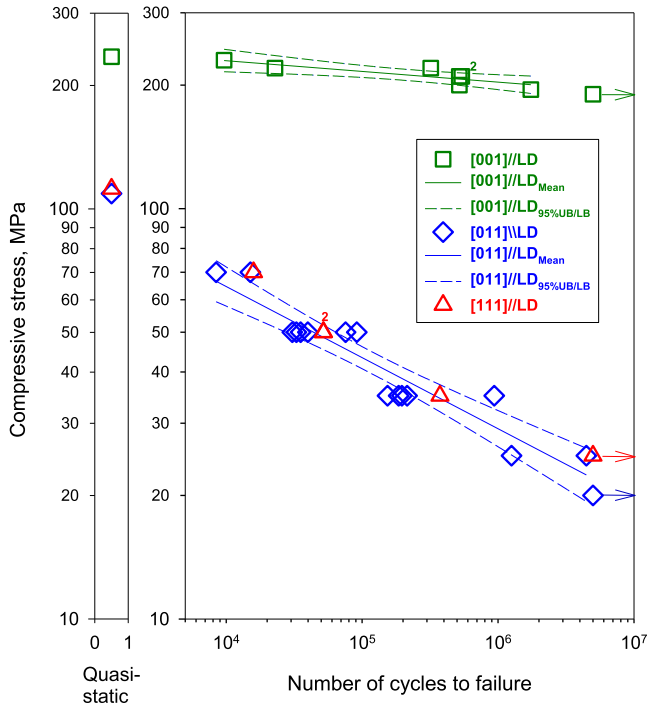

Fig. 5. S–N, maximum compression stress ($\sigma_M = |\sigma_{min}|$ with R = 10) plotted against failure cycle number (N), plots for [001]//LD, [011]//LD and [111]//LD samples. σ_{UCS} values (Huang et al., 2024) are also plotted on the left side of the S-N graph.

a front view image and the right is a 45° view image, respectively. The FP (thus the collapsed plane) being (001) can be seen in the front view image, as pointed to by the arrow, and the portion of lattices above FP has dislocated slightly to the right after collapsing. This is similar to the observation made on the failure of SC [001]//LD lattices reported by others (Radlof et al., 2021; Raghavendra et al., 2021; Li et al., 2014). For the sample viewed at 45°, little sideway movement is observed. Thus, FD in this fractured (001) is parallel to the 45° viewing direction and the FD is [110]. For the [011]//LD sample as shown in Fig. 7b (right) where FVD_S = [100], it can be seen that FP is also (001) with FD = [010] and α = 45°. Thus, fracturing and collapsing have caused the top portion to slip slightly in the (001) FP and in [010], before the test was stopped.

For the [111]//LD quasi-static tested sample (Fig. 7c, photo images1-4), Image 1 is a FVD_S image with α ~ 36°. The four-cell area/rectangular of (110) outlined in the left image (before testing) has been placed in Image 1 of the tested sample and is seen fitted well. The long edge of this four-cell rectangular is [1 $\bar{1}$ 0] parallel to FD or it can be stated that a line parallel to the long edge lies in FP and the short edge of the rectangular is [001] normal to FP. Thus, FP is (001). Image 2 in Fig. 7c is the view after having rotated clockwise the sample in Image 1 for ~45°, displaying the half of the FP edge more clearly. Rotating the sample for a further ~45° (Image 3), meaning the sample in Image 1 having rotated ~90°, and then another 45° (Image 4) have illustrated that vertically the sample has dislocated little. This is reasonable as a shear fracture in [1 $\bar{1}$ 0] in (001) as in Image 1 would cause little dislocating that can be viewed in Images 2 and 4 and no dislocating in Image 3.

FP and FD of fatigue-tested samples are now presented, first for [001]//LD samples. For the test with σ_M = 230 MPa = 0.98σ_{UCS} (Fig. 8a), the slight distortion/bending is similar to that in the quasi-static tested sample in Fig. 7a, but without fracturing. The slight bending should be a gradual process, consistent with the Δd_p in Fig. 4a for the sample having continuously increased as the test cycle increased. The sample (Fig. 8a) did not collapse but the gradual distortion/bending has led Δd_p to reach the m level resulting in the test being stopped and thus "failure" of the sample. For σ_M = 220 MPa = 0.94σ_{UCS}, as shown in Fig. 4a, the failure behaviour is different to that observed in the 230 MPa sample as there is not a gradual increase in Δd_p but a clear and small Δd_p jump associated with the failure in the sample. Correspondingly, Fig. 8b displays the sample having not experienced a high degree of distortion before failure. For all other [001]//LD samples with σ_M < 220 MPa except the runout sample, the Δd_p jump (Fig. 4a) is clear and the level of distortion (Fig. 8c and d) is low. However, in the two low σ_M and thus high N samples in Fig. 8c and d, a few cells have broken away.

For [001]//LD samples, a higher m value may have caused a slightly more noticeable bending but still no collapsing, as shown in Fig. 9a. For [011]//LD and [111]//LD samples, the use of a higher m value has resulted in the samples to fracture completely, providing a clear view of

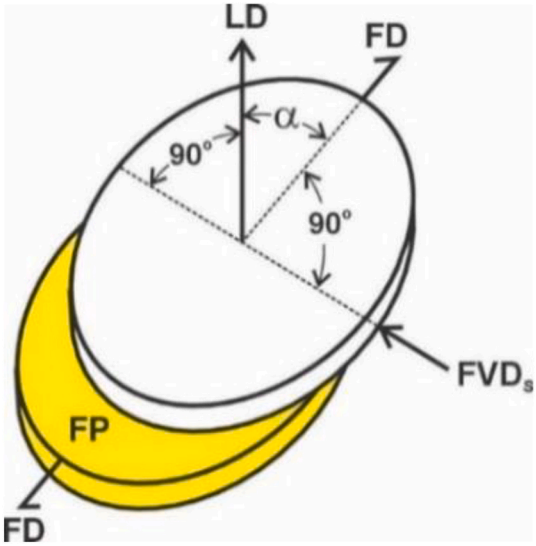

Fig. 6. Schematic illustrating the top and bottom portions represented by the top and bottom disks, respectively, shear fractured along the fracture plane (FP) and the fracture direction (FL) together with a specific front view direction (FVD_S) and ∠LD/FD (as α).

Table 2
Comparison of strength values for the three orientations under quasi-static test condition and at cyclic loading to 10^4 and 10^6 cycles.

Quasi-static		$N = 10^4$		$N = 10^6$	
$\sigma_{UCS[001]} = 235MPa$[a]		$\frac{\sigma_{UCS[001]}}{\sigma_{M10^4[001]}} \approx \frac{235MPa}{230MPa} =$	1.02	$\frac{\sigma_{UCS[001]}}{\sigma_{M10^6[001]}} \approx \frac{235MPa}{201MPa} =$	1.17
$\sigma_{UCS[011]} = 109MPa \approx \sigma_{UCS[111]} = 112MPa$[a]		$\frac{\sigma_{UCS[011]}}{\sigma_{M10^4[011]}} \approx \frac{109MPa}{70MPa} =$	1.56	$\frac{\sigma_{UCS[011]}}{\sigma_{M10^6[011]}} \approx \frac{109MPa}{23MPa} =$	4.74
$\frac{\sigma_{UCS[001]}}{\sigma_{UCS[011]}} \approx \frac{235MPa}{109MPa} =$	2.2	$\frac{\sigma_{M10^4[001]}}{\sigma_{M10^4[011]}} \approx \frac{230MPa}{70MPa} =$	3.3	$\frac{\sigma_{M10^6[001]}}{\sigma_{M10^6[011]}} \approx \frac{201MPa}{23MPa} =$	8.7
$\frac{\sigma_{UCS[011]}}{\sigma_{UCS[111]}} = \frac{109MPa}{112MPa} \approx$	1	$\frac{\sigma_{M10^4[011]}}{\sigma_{M10^4[111]}} \approx \frac{70MPa}{70MPa} =$	1	$\frac{\sigma_{M10^6[011]}}{\sigma_{M10^6[111]}} \approx \frac{23MPa}{22MPa} \approx$	1

[a] Data cited from Huang et al. (2024).

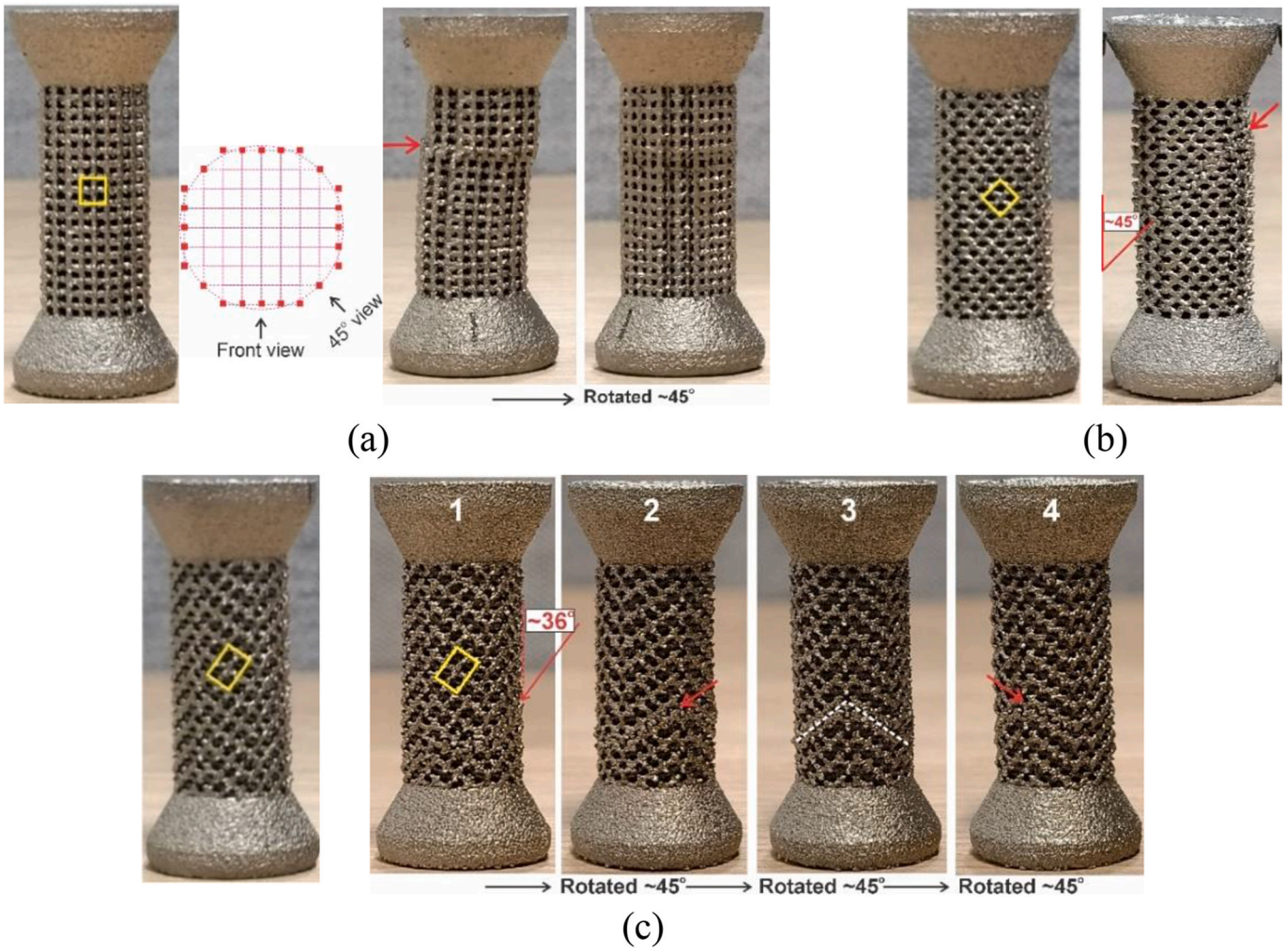

Fig. 7. Photographs of a pair of (left photo for untested and right photo/photos for quasi-static tested) samples: (a) [001]//LD with a schematic illustrating a cross-section normal to LD, the outer nodes in red, and viewing directions, (b) [011]//LD, and (c) [111]//LD samples. Notes: The yellow square or rectangle represents 4 unit cells and arrows point to the fracture paths. The angles between FD and LD in (b) and (c) are indicated.

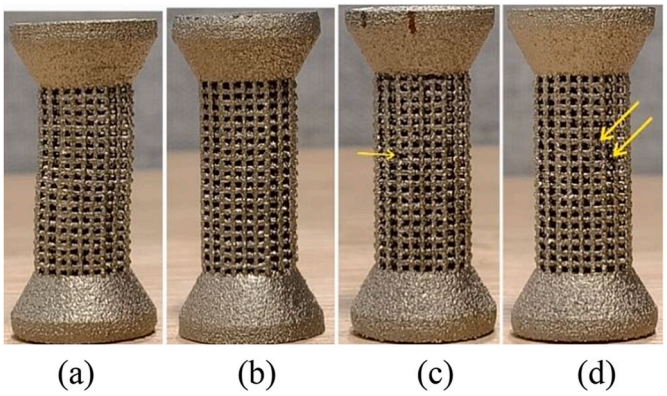

Fig. 8. Photographs of [001]//LD fatigue tested (m = 92 %) samples, with σ_M= (a) 230 MPa, (b) 220 MPa, (c) 200 MPa, (d) 190 MPa. Arrows point to cells broken or fallen out.

FP and FD. This is despite the insignificant effect on N, as shown in Fig. 4. Using m = 92 %, the failure associated with FP moving along FD has taken place and thus there was a Δd_p jump to cause the stop of the test, which is evident in Fig. 4. However, for m = 92 %, the Δd_p jump must be insufficient for the samples to have completely fractured (Fig. 9b-right). The use of a higher m value has caused fracturing/sliding further, thus separating the fractured pieces, as shown in the left sample of Fig. 9b-left for the [011]//LD sample. The FP is (001) and the FD is [010] or [0 $\bar{1}$ 0], 45° to LD. The FP and FD of the fatigue tested [011]// LD samples are thus the same as those identified for quasi-static samples explained earlier.

For [111]//LD samples, with the higher m value, the more severely fractured sample in Fig. 9c (left image) shows FD at ~36° to LD in FVD_S viewing. This is exactly the same angle as the one that has also been identified for the quasi-static tested sample shown in Fig. 7c, although the height of the FP in the two samples differ, meaning fracturing in different (001) layers. After rotating the fractured [111]//LD sample 90° from FVD_S, the image in Fig. 9c (mid) for the cyclic loading tested sample is very similar to Image 3 in Fig. 7c for the quasi-static sample and shows little dislocating vertically. This also confirms that FP is (001) and FD is [1 $\bar{1}$ 0] in cyclically tested [111]//LD samples. Table 3 summarises the geometrical features (FPs, FDs and α values) of fracturing in the different cell-orientated lattices. How fracturing in these lattices had initiated locally in cells under cyclic loading is presented next.

3.3. Crack initiation observed on surfaces of tested samples

Firstly, a SEM image for a quasi-static tested [001]//LD sample is presented in Fig. 10a. There are four rows of horizontal struts although

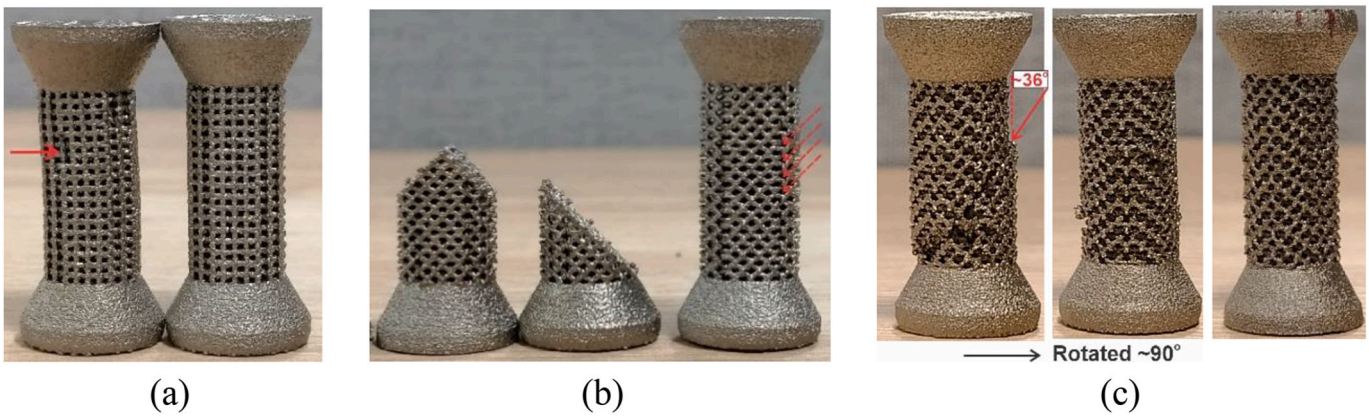

Fig. 9. Photographs of fatigue tested (a) [001]//LD samples (210 MPa), left with m = 150 % and right with m = 92 % and the arrow pointing to local cells broken and fallen out, (b) [011]//LD samples (50 MPa), left with m = 135 % and right with m = 92 % and arrows pointing to cells with shared deformation identifiable, and (c) [111]//LD samples, left with m = 135 % fracture in a plane ~36° to LD and right with m = 92 %.

Table 3
Fracture plans, fracture directions and fracture sliding angles of the three different cell orientated lattices.

Sample	FP-FD	α (∠FD./LD)
[001]//LD	(001)-[110]	90°
[011]//LD	(001)-[0 $\bar{1}$ 0]	45°
[111]//LD	(001)-[110]	35.3°

the top and bottom rows are only partial in the image. Four rows of struts should include three rows of pores, however, only two rows of pores are seen. This is because the vertical struts in a row (mid-row in Fig. 10a) have collapsed so that the pores have been pressed "closed" making them no longer visible from the front. Note also the top two rows of struts are not vertically aligned with the vertical struts in the bottom two rows. This is because the top part of the sample has moved sideways by a half-cell distance viewed from the front. As has been explained and illustrated in Fig. 7a, the collapsing and sliding in (001) and along [110] has resulted in the top part having moved $\sqrt{2}\ a_{Cell}/2$ along the 45° viewing direction and $a_{Cell}/2$ along FVD_S. An important feature of the quasi-static tested sample shown in Fig. 10 is that, in cells above or below the fractured (001), there are no microcracks observed.

SEM examination of the fatigue-tested sample, shown in Fig. 10b, has revealed that the sample failed without a significant amount of distortion, without fracturing in a whole plane and thus without collapsing. However, as shown in Fig. 4a, there was a small Δd_p jump in the sample tested using m = 92 %. This jump should be the result of a sudden displacement within a very small number of cycles. Examining carefully the tested sample surface has revealed that cracks have locally well initiated, as shown in Fig. 10b. Cracks can be seen in horizontal struts and one strut is shown to have fully fractured. It is possible that, when a horizontal strut has fractured the vertical struts next may effectively become longer struts/columns and thus buckling more readily to occur. Thus, it is possible that when a horizontal strut breaks, vertical struts nearby can be compressed (buckling) more readily leading to the 92 % tolerant level being reached, causing the test to stop correspondingly.

Examination of a quasi-static tested [011]/LD sample (Fig. 11a) has shown that the struts fractured in (001) along [100]. However, because [011] is parallel to LD in [011]//LD samples, the fractured (001) is at 45° to [011] and also to LD, viewed from the front. The global view of this has been shown in Fig. 7b. Also similar to the [001]//LD sample, there are no cracks observed in cells next to the fractured (001) in the quasi-static tested [011]//LD sample. Very different to the quasi-static tested [011]//LD sample, as shown in Fig. 11b, a large number of

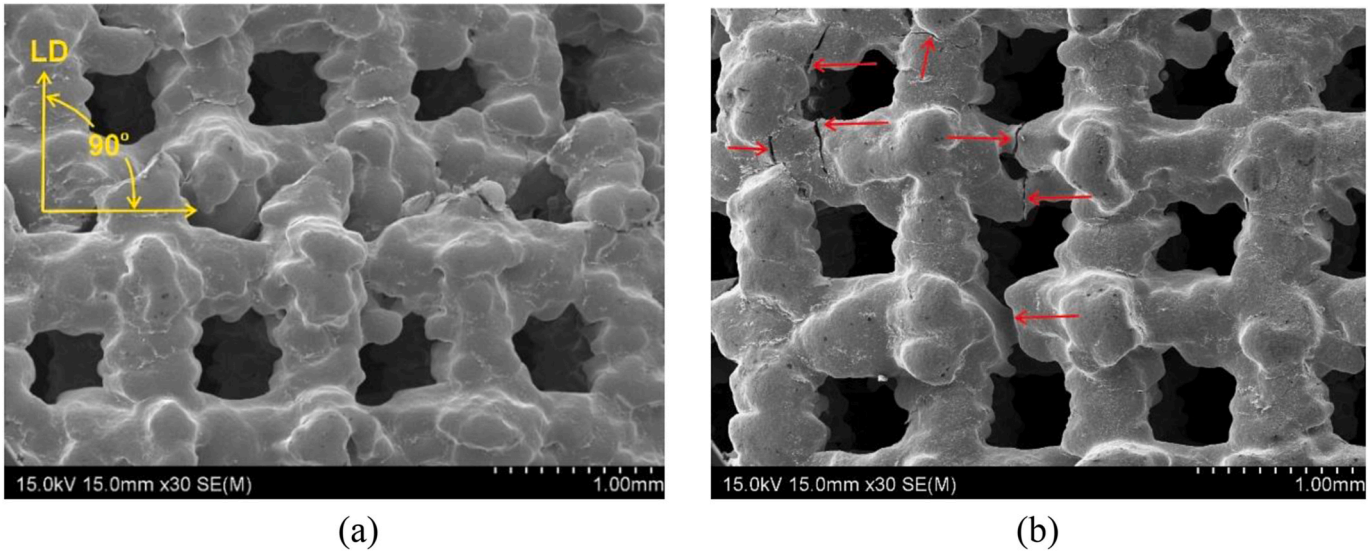

Fig. 10. SEM surface images of [001]//LD samples, (a) quasi-static tested with fracture plane to LD being ~90° indicated, (b) cyclically tested at 210 MPa with arrows pointing to cracks.

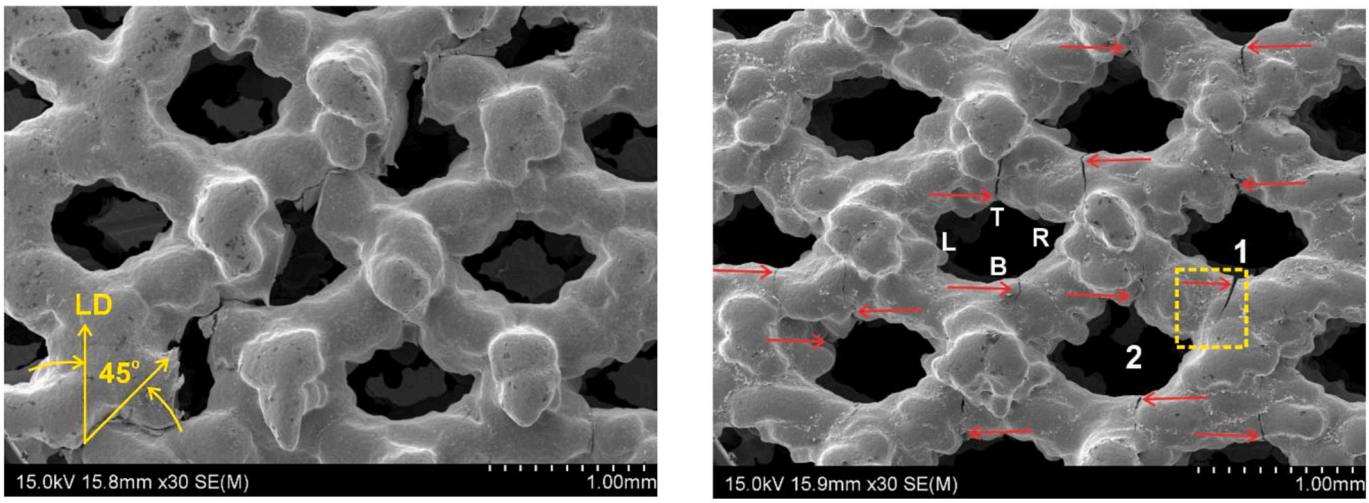

Fig. 11. SEM surface image of [011]//LD samples: (a) quasi-static tested and (b) tested at 50 MPa with m = 92 % showing cracks having initiated in T and B locations of strut nodes, as pointed to by red arrows.

small cracks can be observed in the fatigue tested [011]//LD sample particularly in locations of the lattice as pointed to in Fig. 7b. Clearly displayed in Fig. 11b is that, locally, crack initiation occurred at or near the top or the bottom corners of each cell, not the left and right corners. However, there is an indication that after a crack has initiated and grown straight down or up for a short distance, the crack propagation may tend to deviate. An example is shown in Fig. 11b that the crack initiated in the bottom of Cell 1 was propagating toward the right of Cell 2.

Fracturing in a [111]//LD quasi-static tested sample as shown in Fig. 12a with the viewing direction the same as that for viewing Image 2 in Fig. 7c, again, occurs without small cracks (microcracks) to be seen next to the main crack. Similar to the [011]//LD sample (Fig. 11b) tested and failed under fatigue loading, small cracks can be seen in the T and B locations of cells in Fig. 12b, although the top and bottom corners are not in the same viewing plane for the [111]//LD sample viewed from the front. This unique feature of crack initiation readily occurring in the top and bottom corners of a cell in the non-[001]//LD samples may well be the reason for the cyclic loading to have adversely and considerably affected the fatigue strength of the lattices, as shown in Fig. 5 and Table 2. On the other hand, in the tests of [001]//LD samples, there are no such locations inside a cell for cracks to easily initiate, if σ_M is not very high. Thus, cyclic loading only slightly affects the strength of [001]//LD samples, as is also shown in Fig. 5 and Table 2.

3.4. Crack initiation and growth observed inside the struts

Crack initiation and growth can be further understood by examining the crack paths internally in struts and nodes after sectioning/preparing the samples and also by examination of the fracture surfaces. The cross-sectional views of [001]//LD samples are shown in Fig. 13. In the quasi-static sample, as has been explained, the portion above the fractured (001) has moved along [110] meaning in 45° direction slightly. Thus, the struts above and the struts below the fractured (001) no longer align. When the bottom portion is polished for the struts below the fractured (001) to be viewed in the cross-section, the vertical struts above cannot be viewed, as shown in Fig. 13a. For the cells that can be viewed in the image, there are basically no cracks in location away from the fractured

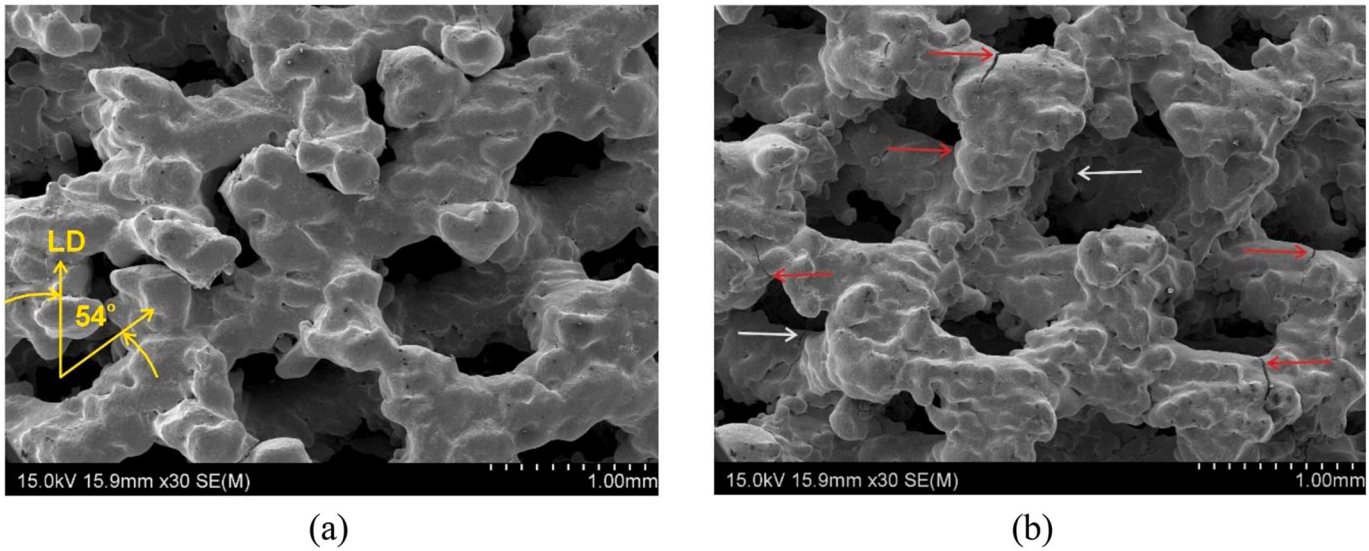

Fig. 12. SEN surface images of [111]//LD samples: (a) quasi-static tested and (b) tested at 50 MPa 92 % showing cracks having initiated in T and B locations of strut nodes, as pointed to by arrows.

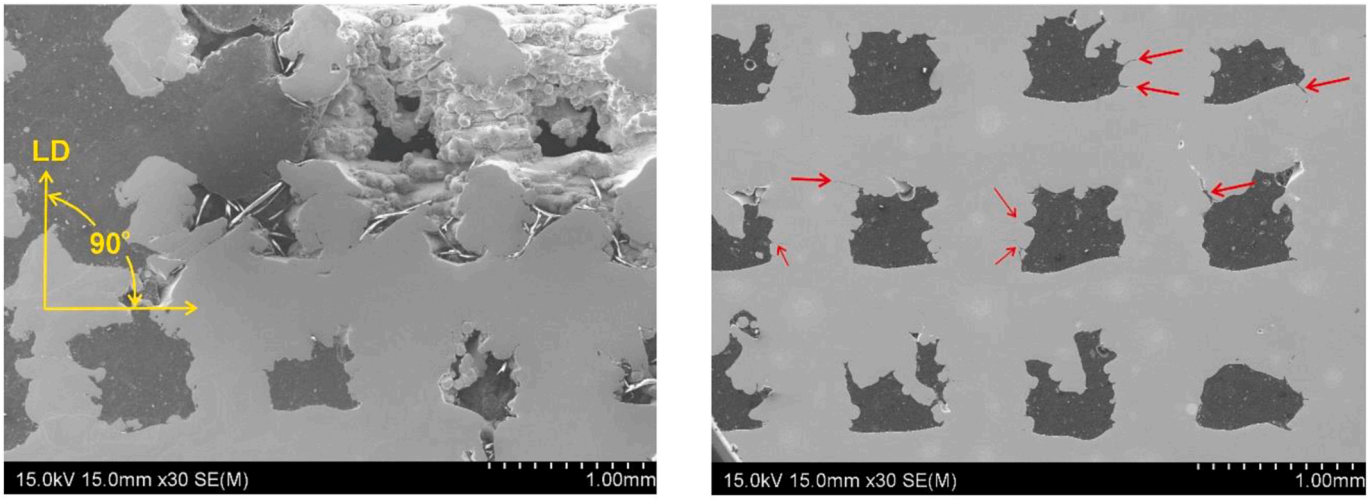

Fig. 13. SEM cross-sectional images of [001]//LD samples, (a) quasi-static tested, (b) cyclically tested at 210 MPa. In (b), microcracks are pointed to by arrows.

(001). This examination of the internal struts shown in the cross-section is consistent with what has been observed by examining the surface of the tested sample in Fig. 10a. For the fatigue tested sample which has not fully fractured and collapsed, some microcracks can be observed, as indicated in Fig. 13b.

Carefully cross-sectioning for examining crack growth inside the struts in a metallographic plane normal to the fractured (001) can be achieved for [011]//LD samples. For [111]//LD samples, sampling cannot be done to view the cross-sectioned struts in a metallographic plane that is normal to FP and also includes LD in the plane. As has been shown, quasi-static and fatigue strength values of [011]//LD samples are very comparable to the values of [111]//LD samples and locations of crack initiation in their samples are similar, as shown in Figs. 11b and 12b. Thus, examining the [011]//LD samples should be sufficient for revealing the crack initiation and growth in these samples. The cross-section of the quasi-static tested sample in Fig. 14a showing the fracture of struts along (001) without displaying microcracks away from the crack path is consistent with what has been observed in Fig. 12a.

For cyclically tested [011]//LD samples, crack initiation in T and B locations can be clearly seen in cross-sections of struts/modes shown in Fig. 14b and c. This is the same as what have been explained from observing the tested sample surfaces. Crack initiation in these locations are seen to be the same for both $\sigma_M = 70$ MPa and $\sigma_M = 35$ MPa, respectively, corresponding to $N \sim 10^4$ and $N \sim 10^6$. In these images, crack paths can be revealed in detail, providing information on how cracks have grown. In both Fig. 14b and c, all the red arrows point to the crack tips with each crack having deviated in growth direction. As indicated in Fig. 14c, the crack initiated in T location of Cell 1, instead of growing upward through the node to Cell 5, has changed direction and has grown towards the L location of Cell 2. The crack deviation is reasonable as a node is significantly thicker than the struct,

As cracks have deviated and cracking has advanced, each crack grew through a struct on one side to the next cell in ~45°. For example, Fig. 14c shows that at the time when the test stopped and the sample failed, the T crack in Cell 1 was growing towards Cell 2, the T crack in Cell 2 was growing towards Cell 3, and the T crack in Cell 3 was growing towards Cell 4. The B cracks in Cell 4 and in Cell 2 also were growing respectively towards Cell 3 and Cell 1. Only the B crack in Cell 3 was growing to Cell 6, but also to Cell 2. The cracks growing and opening along Cell 1 to Cell 4 must have resulted in the relative moment Δd in direction d as indicated in Fig. 14c, and when $\Sigma\Delta d \times \cos 45^\circ = \Delta d_p$, the test stopped. Increasing m value would allow a higher Δd value and if the m was sufficiently high, complete cracking into two pieces of the sample would result. The actual fracture path is thus through the strut node in each cell along a (001) plane.

The fracture surface of a completely fractured sample has been further studied by examining the fractured struts in a fractured [011]// LD sample, shown in Fig. 15. The viewing direction is normal to the fractured (100). Thus, a unit cubic cell appears cubic on the fractured surface. The fracture of the plane has resulted from the fracture of all the nodes or near in that plane. Nodes 1 and 2 in the left image of Fig. 15 can be examined better in a higher magnification, centre-top image. The appearance of each node is similar, as both node 1 and node 2 in the image have shown, consisting of two sections, meaning failure through two stages. This can be more readily seen in a higher magnification image showing only one fractured note, top-right image. In the first section (from location a), the apparently flat crack plane appearance suggests the crack propagated smoothly in one direction until reaching location b. Then, the crack seems to have changed direction. This change in the crack growth direction is consistent with the crack growth path deviation observed in cross-section of struts and nodes, as already illustrated and explained above.

The two stages of crack growth in each node can be better shown with a further higher magnification in locations “a” and “b” (the bottom two images in Fig. 15). Location “a” is where the crack initiated, with the red dotted line representing the front of the crack initiation, showing the fracture mode being brittle with little shear dimple appearance. The crack then propagated to location “b” where stage I crack transited to stage II at the boundary as outlined by a white dotted curve in the image in lower-left image of Fig. 15. After the boundary and the change of crack growth direction, the fracture is a ductile one with shear dimples decorated the fracture surface. This suggests that stage I is the fatigue crack growth and stage II is the sudden fracture when the remaining supporting area of the strut area adjacent to the node after stage I can no longer support σ_M, causing rapid fracturing in the strut section.

3.5. *Estimation and effect of stress concentration*

To understand the location sensitivity of crack initiation, stress distributions are estimated by simulation. The simulation is not intended to predict the fatigue life, meaning that neither the number of cycles for crack initiation nor the total number of cycles when the sample failed were attempted to be predicted. Rather, the simulation using σ_M values to estimate stress distributions is for identifying the locations of high

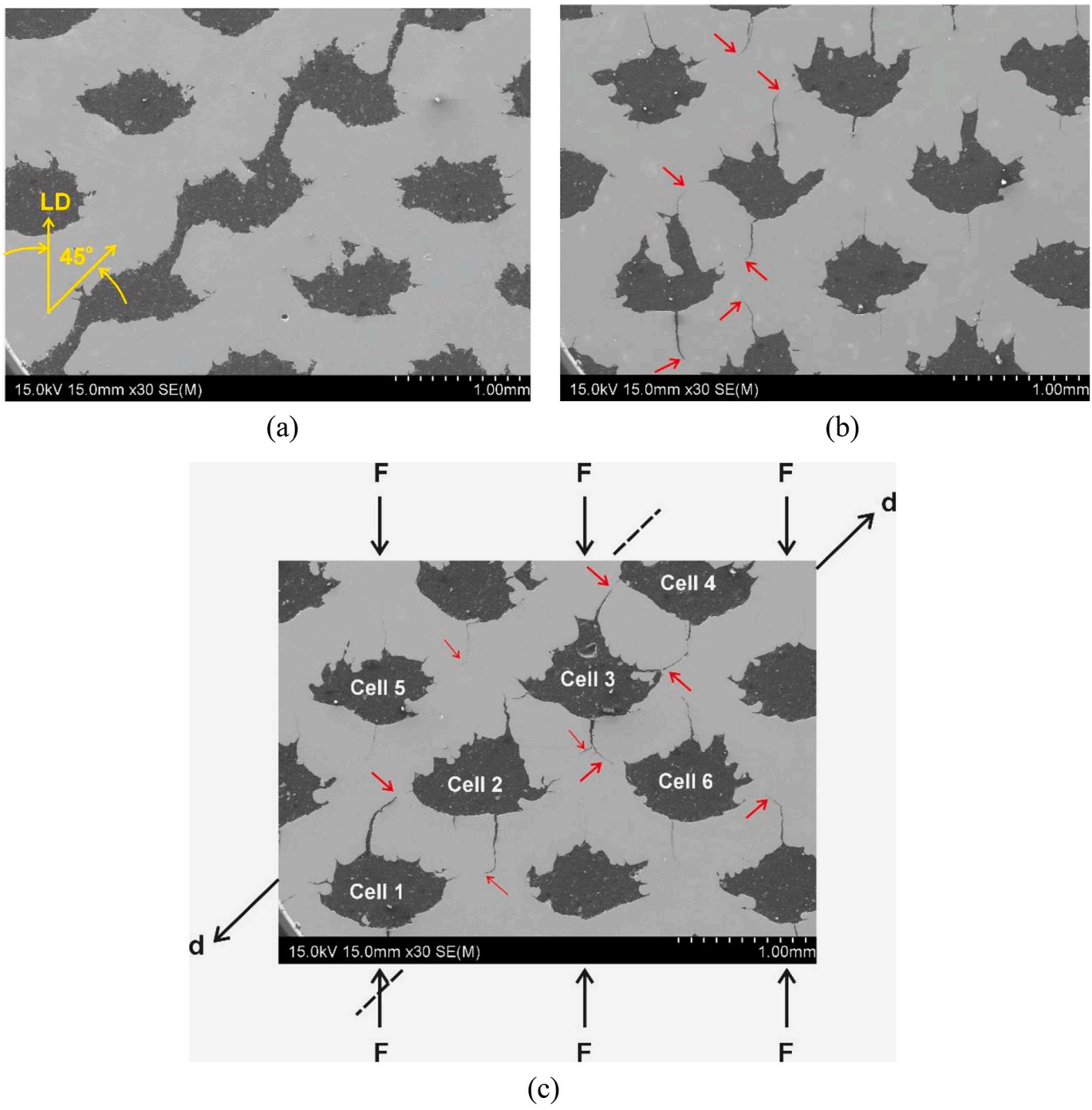

Fig. 14. SEM cross section images of [011]//LD samples showing, (a) a main crack path in a quasi-static tested sample without microcracks away the main crack, (b) and (c) cyclically tested under 70 PMa and 35 MPa, respectively, displaying many small cracks having initiated and grown. In (b) and (c) red arrows point to the cracks with the cracks growing away from the vertical direction. In (c), loading and possible shear displacement are indicated.

tension and thus for understanding the condition for crack initiation. As shown in Fig. 5, for [001]//LD samples at $N = 10^6$, $\sigma_M \sim 200$ MPa. For both [011]//LD and [111]//LD samples at $N = 10^6$, $\sigma_M \sim 35$ MPa. Simulated stress distributions based on these σ_M values to reveal the distributions of the first and the third principal stresses (σ_1 and σ_3) values are shown in Fig. 16. The location and magnitude of σ_1 and to a less-extent σ_3, if positive, may provide a mechanic reason to explain the locations of crack initiation that have been observed.

For the [001]//LD with $\sigma_M = 200$ MPa, as shown in Fig. 16a, σ_1 is close to zero and σ_3 is high and negative in vertical struts, reasonably showing that the vertical struts dominantly support the compressive loading. This is the reason that the vertical struts in Fig. 16a have appeared slightly bulged as $\sigma_M = 200$ MPa is higher than the apparent 0.2 % yield stress of the lattice (at 182 MPa [45]). In horizontal struts away from the nodes, both σ_1 and σ_3 are close to zero meaning close to be stress-free. But, moving towards the nodes in horizontal struts, σ_1 increases meaning that tension increases. In the locations next to nodes σ_1 is up to 530 MPa. The high (positive) σ_1 value in horizontal struts near the nodes predicted in the simulation may explain the cracks locally observed in the horizontal struts, as shown in image of Fig. 10b in the sample tested under a cyclic load.

For [011]//LD with σ_M only at 35 MPa (considerably lower than the

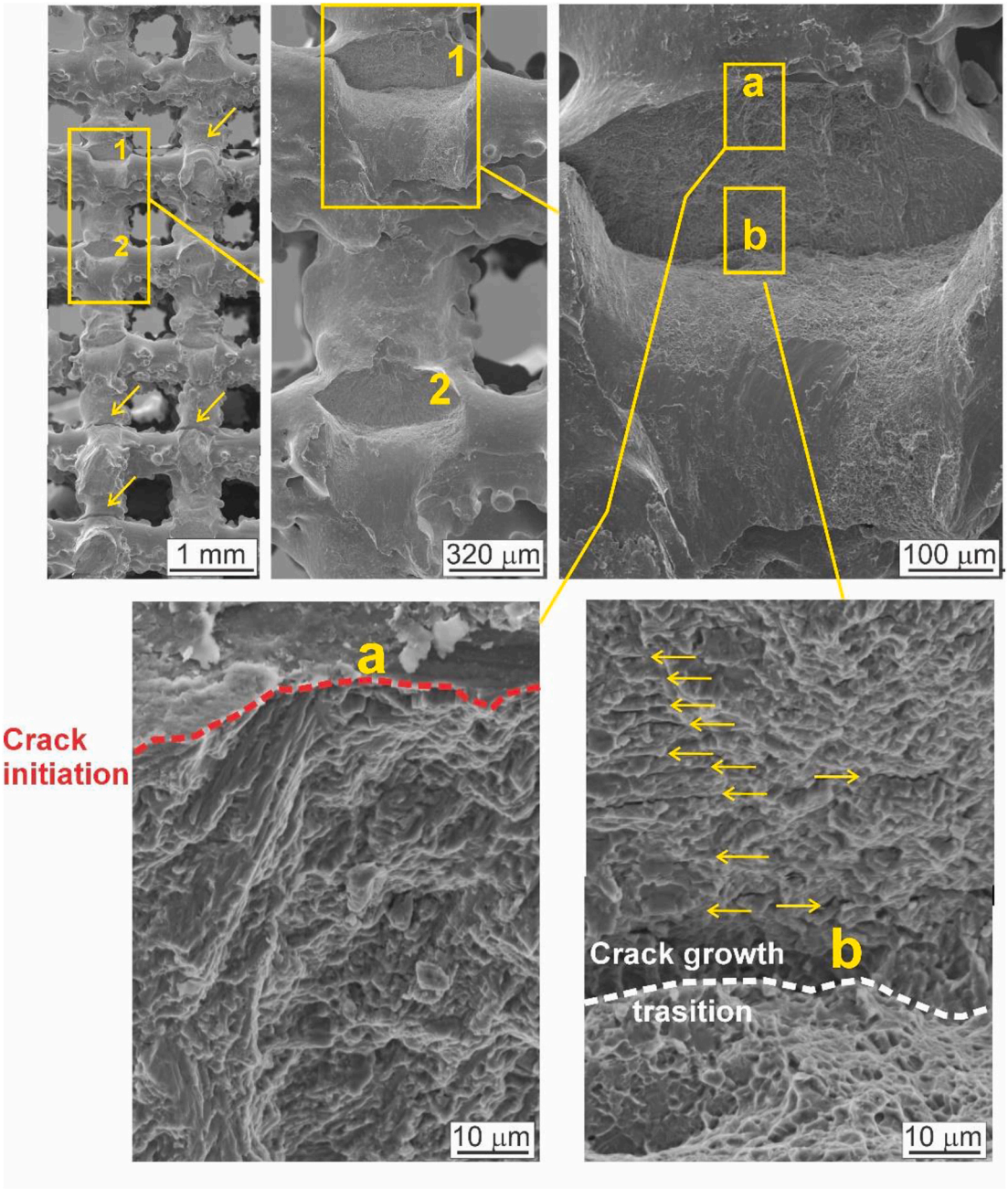

Fig. 15. SEM fractography of the [011]//LD sample as shown in Fig. 9b-left, with viewing direction normal to the fractured (100) fractured plane. Arrows point to microcracks. Crack initiation front and crack growth transition front are indicated by dotted curves.

apparent yield stress of the lattice at 92 MPa (Huang et al., 2024), as shown in Fig. 16b, the lower and upper corners of each cell are high tensile stress concentration locations with σ_1 reaching ~586 MPa. The rest in each cell is largely under compression supporting the applied load and the left and right corners are high compression stress concentration locations with $\sigma_1 < -326$MPa. Under this stress distribution and under cyclic loading condition, cracks initiating in upper and lower corner locations as observed and shown in Fig. 11b is reasonable. Stress distribution of [111]//LD (Fig. 16c) is similar to [011]//LD (Fig. 16b), in that the upper and lower corners of each cell are high and positive σ_1 concentrated locations, with the maximum value of σ_1 at approximately 513 MPa. Thus, cracks also initiate in the upper and lower corner locations, as shown in Fig. 12b.

At 10^6 cycles, σ_M values are close to fatigue limits for high cycle fatigue (HCF). As is understood (Schijve, 2009) [52], the stress concentration factor is the primary factor for crack initiation during cyclic loading and the fatigue limit represents the stress level under which crack initiation at the root of a notch does not occur. In effect, all the corner locations of the lattices may be viewed as notches. The high stress (σ_1) concentration in the top and bottom corner locations of each cell in [011]//LD and [111]//LD samples reaching respectively 50–60 % of σ_y, (yield strength of the alloy) when $\sigma_M \sim 35$ MPa, have resulted in cracks well initiated in some of these locations after a high number (10^6) of cyclic loading. For [001]//LD samples, even when $\sigma_M = 200$ MPa (higher than the yield stress of the lattice sample), σ_1 in notches (corner locations) has only reached slightly over 500 MPa. Thus, for [001]//LD samples, cyclic (compression) loading has only slightly affected the fatigue strength, and the strength is high. It is also understood that the notch effect on crack initiation is small or negligible in the quasi-static loading condition (Li et al., 2014). Thus, it is also reasonable that

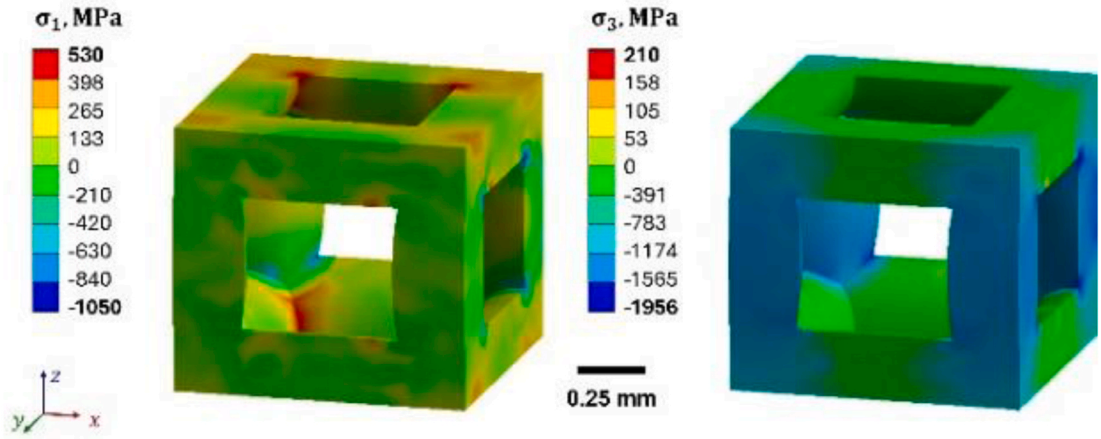

(a)

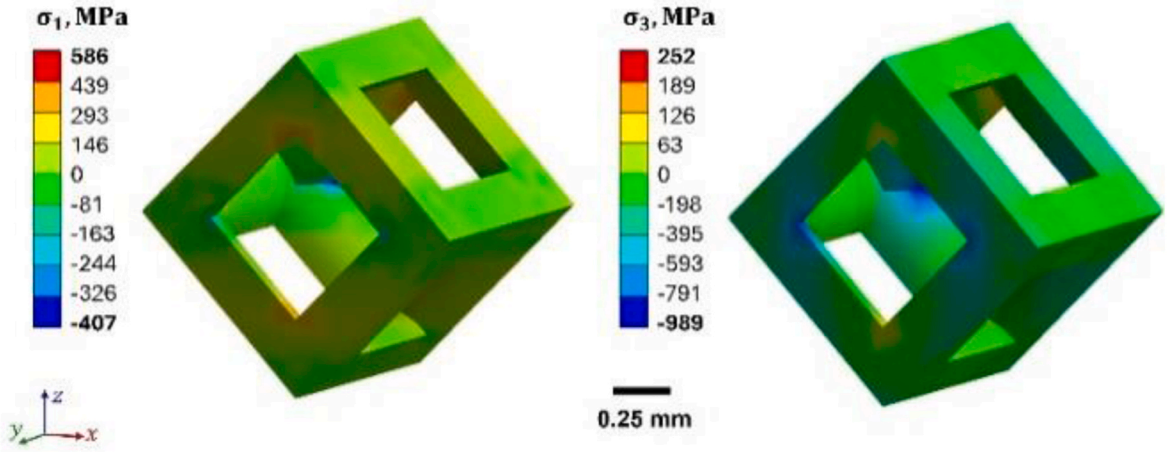

(b)

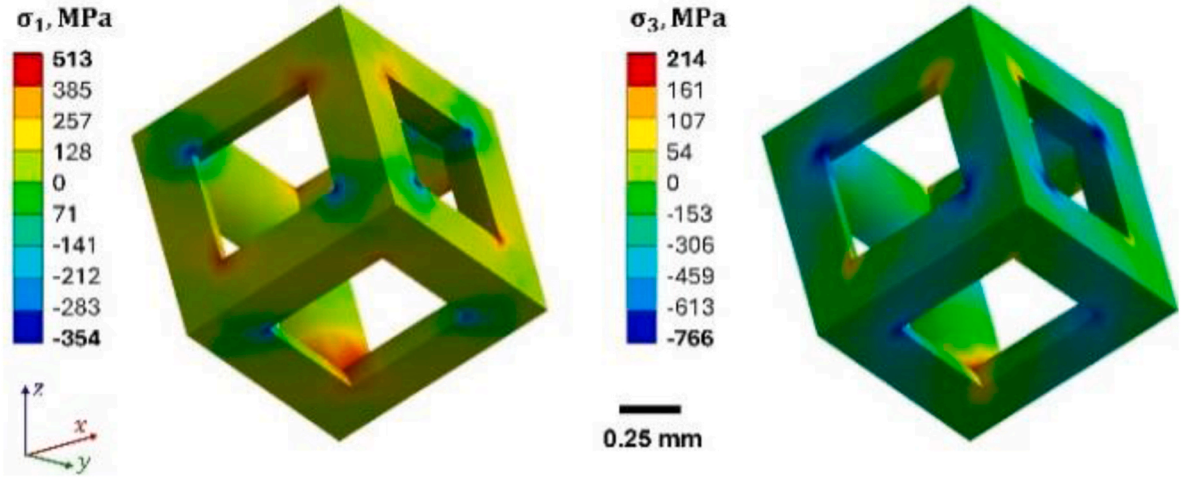

(c)

Fig. 16. Distributions of principal stresses, σ_1 and σ_3, under a static apparent applied stress (σ_{ap}) for (a) [001]//LD lattice when $\sigma_M = 200$ MPa, (b) [011]//LD lattice $\sigma_M = 35$ MPa, and (c) [111]//LD lattice when $\sigma_M = 35$ MPa.

there are no microcracks observed away from the main cracks in quasi-static tested samples.

3.6. Further discussion on fatigue strength of PBF lattice structures

The role of crack initiation locations in PBF lattice structures to lower the fatigue strength of the structures identified in the present study can be used to explain the literature data that has been briefly reviewed in Introduction. For this, the S-N data for PBF lattice structures with designed ρ_r between 0.3 and 0.4 stated in the various studies in the literature have been plotted in a single S-N graph, shown in Fig. 17. In the graph, for comparison, the S-N trend curves from this study based on the S-N data plotted in Fig. 5 are included. In Fig. 17 (left), same as in Fig. 5 (left), σ_{UCS} values from various studies and from our previous study have also been plotted. One trend curve has been drawn and one σ_{UCS} value has been provided to represent both [011]//LD and [111]//LD samples from this work. This is because the curve fits all the S-N data from samples of the two different orientated cell lattices well and σ_{UCS} of [011]//LD samples is very close to that of [111]//LD samples. As shown in the figure, the fatigue strength values of [001]//LD samples in the present work are significantly higher than all the strength values reported in literature for that relative density range.

Fig. 17 shows that, for [001]//LD samples, strength values from Zhao et al. (2016) and from Radlof et al. (2021) are significantly lower than the strength values determined in this study. The reasons for these differences need to be considered. In Zhao et al.'s work, ρ_L of SC lattice samples is stated to be 1.63 g/cm^3 (thus relative density $\rho_L/\rho_S = 0.37$). However, as they have stated, their designed strut diameter (thickness) is 0.5 mm and cell size is 10mm/7 = 1.43 mm. Then, it can be calculated that $\rho_L/\rho_S \sim 0.28$ in their design, which is significantly lower than the designed ρ_L/ρ_S value (being 0.36) in the present work. The fatigue strength estimated from Zhao et al.'s data in Fig. 17 trending towards ~120 MPa, compared to the fatigue strength of 190 MPa from the work for [001]//LD samples may thus seem reasonable. In Radlof et al.'s work, from the data they have provided that strut thickness being 0.6 mm and pore size being 1.2 mm, $\rho_L/\rho_S \sim 0.26$, lower than their stated value of 0.3 and slightly lower than Zhao et al.'s $\rho_L/\rho_S \approx$ value (0.28).

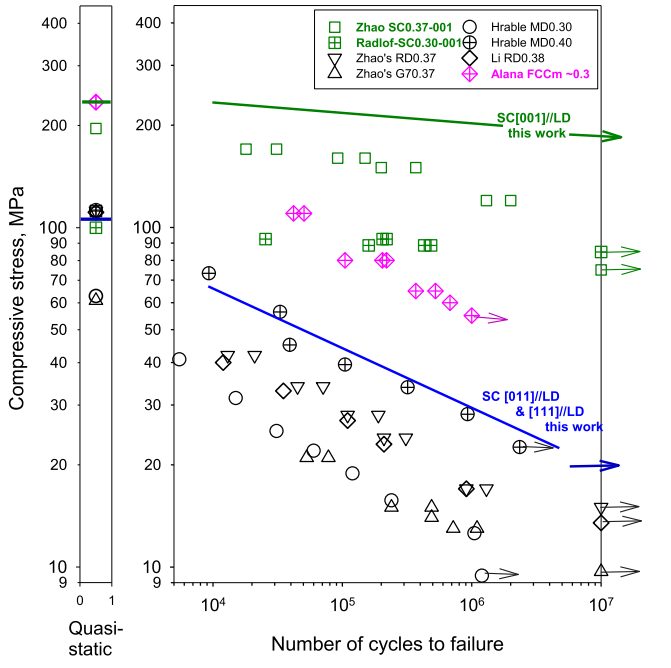

Fig. 17. σ_M-N curves (with R = 10) from the present work with σ_M-N data available from literature plotted in the same σ_M-N graph. σ_{UCS} values (Huang et al., 2024) are also plotted on the left side of the σ_M-N graph.

However, it is not clear why both Radlof et al.'s quasi-static strength and fatigue strength values in the whole high cycle range are significantly lower than Zhao et al.'s values. Note Zhao et al.'s S-N data show that σ_M does not decrease steeply as N increases. Radlof et al.'s data show that σ_M is very weakly dependent on N.

For non-SC lattices except for the values for FCC$_m$, Fig. 17 shows that both quasi-static and cyclic strength values of all non-SC lattice structures are close to or lower than the strength values of the SC non-[001]//LD lattice samples from this work. It may be suggested that, for all the non-SC lattice structures, there may always be various fractions of struts supporting the load quite non-vertically and thus there may always be high stress concentration locations even when σ_M is not high. Thus, supporting the load in non-SC lattice structures may be quite similar to supporting the load in SC non-[001]//LD lattice structures, considering the effect of stress concentration on fatigue strength. Thus, non-SC lattice structures are considerably weaker than SC-[001]//LD structures under cyclic loading. Fig. 17 also shows the effect of ρ_r on the fatigue strength. This is demonstrated by observing Hrabe et al. (2011) data. Their $\rho_r = 0.4$ (both quasi-static and cyclic) strength values are almost exactly the same as the values from this work for SC/non-[001]//LD samples. Their $\rho_r = 0.3$ strength values are much lower.

The exception regarding FCCm from Alaña et al. (2021) is now discussed. They modified the cell design for the purpose of avoiding the "manufacturing problems" associated with building horizontal struts. The design of FCCm, as they have shown, has effectively resulted in each of all the struts supporting the load at 45° to LD, with four struts joining in each node. Referring to Fig. 2, for SC [001]//LD lattices, the 4 vertical struts effectively and the 8 horizontal struts do not effectively support the load in each cell. For [011]//LD samples, 4 horizontal struts do not effectively and 8 struts effectively support loading with each in 45° to LD. For [111]//LD, all 12 struts support loading effectively, with each in 54.7° to LD. For FCCm, all struts support load effectively, with each 45°to LD. The lower angle to LD (than that in SC-[111]//LD lattices) should result in supporting a higher load before yielding and before fracture under quasi-static loading. It can be shown, by simulation, $\sigma_{y\text{-}FCCm}$ (yield stress) reaches 175 MPa for $\rho_L = 0.3$. Simulation predicted $\sigma_{y\text{-}[001]//LD} = 172$ MPa, $\sigma_{y\text{-}[011]//LD} = 103$ MPa and $\sigma_{y\text{-}[111]//LD} = 98$ MPa and these values agreed with experimentally determined values closely (Huang et al., 2024). Thus, a high σ_{UCS} value of FCCm at 234 MPa is also reasonable. However, as is clear in Fig. 17, under cyclic loading and as N increases, σ_M decreases sharply. This is because there are T and B locations being highly stress concentrated in an FCCm lattice, favourable for crack initiation and thus resulting in a rapid decrease in σ_M as N increases under cyclic loading.

The location-dependent crack initiation sites that have been observed may have also provided an indication of how the surface quality of PBF lattices may affect fatigue limits. Cross-sections of samples in Figs. 13 and 14 have been presented in a way that the build direction is pointing upwards. This means the lower surfaces in cells of [001]//LD samples or the bottom corners of cells in [011]//LD samples are top surfaces, and all others are side surfaces during EBPBF. As can be observed in Figs. 13 and 14 and as is well understood, the top EBPBF surfaces are considerably smoother than the side surfaces. This is because the side surfaces are partially melted particle surfaces and the EBPBF top surfaces are the solidified surfaces without the original powder particles. The high roughness of side surfaces in PBF parts/samples is known to adversely affect fatigue strength. However, Figs. 11b–12b and 14b and c have shown that crack initiation sites are primarily the T and B cites of cells and B locations appear as readily as T locations to initiate cracks under cyclic loading. This strongly suggests that stress concentration is the dominant factor when the fatigue strength of lattices is considered, while surface quality is not highly significant in this case.

3.7. Limitations and perspectives for future work

There are a number of limitations in the present study. Firstly, as has been explained (in 3.5), the simulation conducted in the present work is limited to static loading and is for understanding the locations where cracks may initiate rather than for predicting fatigue performance. Secondly, all comparisons to non-SC lattices have been based on data and trends that are available in literature. The present study has focused on SC latices so that the orientation effect on fatigue performance can be evaluated, and testing of non-SC lattices has not been conducted. Thirdly, manufacturing-defects have not been specifically considered although, as has been explained in the previous section, our data and observations have suggested that high stress concentration locally is the dominant factor to initiate cracks and thus to shorten the fatigue life.

In future studies, fatigue performance under multiaxial and variable-amplitude loading conditions should be considered as in implant service there are conditions rather than just axial loading with a single R value. In the present work, stress distributions of lattices relating to crack initiation and fatigue performance have been studied and identified. This knowledge is important for lattice design. However, how the grain structure and the microfeatures of the two microconstituents (α and β phases of the alloy) that are specific to EBPBF may relate to the crack initiation and growth have not been considered. This should be revealed in future studies. Furthermore, atomistic simulation to connect the crack initiation mechanism to dislocation motion and slip activity could complement the FE models. This could provide an insightful understanding of the crack growth behaviour from studying the interplay between the lattice geometry and the intrinsic material-level deformation and failure.

4. Conclusions

In this study, how the loading direction (LD) in combination with unit cell orientation of simple cubic (SC) Ti6Al4V lattice structures made using EBPBF on the fatigue strength of the structures under cyclic compressive loading, using R = 10, are studied. The conclusions are:

1. Fatigue strength of [001]//LD lattice decreases moderately from $\sigma_{UCS} = 235$ MPa tested under quasi-static condition to the run-out value of $\sigma_M \sim 190$ MPa when the lattice is cyclically tested to 5×10^6 cycles.
2. Fatigue strength of either the [011]//LD lattice or the [111]//LD lattice decreases rapidly as the fatigue life cycle increases, from $\sigma_{UCS} \sim 110$ MPa under the quasi-static condition to $\sigma_M \sim 70$ MPa tested to 10^4 cycles and to $\sigma_M \sim 25$ MPa tested to 5×10^6 cycles.
3. The low fatigue strength of the non-[001]//LD lattices has been found to be the result of crack initiation and growth readily occurring in the higher-tension locations, which are the top and bottom locations of each unit cell. In the [001]//LD lattice, there are no such locations and thus its fatigue strength is high.
4. In the non-[001]//LD samples, once initiated and grown for a short distance in the nodes, each crack propagates sideway to the left or the right towards the neighbouring cells leading to lattice fracturing along (001). For the [001]//LD condition, the lattices do not fracture and failure leading to the test stop was due to the lightly local compression movement likely as the result of local cracking under high cycle fatigue test conditions at high σ_M.
5. All available data in the literature show that high cycle fatigue strength values of non-SC lattice structures are low, with $\sigma_M \leq 25$ MPa. This is because in these lattices, the same failure mechanism as that identified for the non-[001]//LD SC lattices in this study must have operated.

CRediT authorship contribution statement

Yawen Huang: Writing – review & editing, Writing – original draft, Software, Methodology, Investigation, Formal analysis. **Zhan Wen Chen:** Writing – review & editing, Writing – original draft, Supervision, Methodology, Investigation, Formal analysis, Conceptualization.

Declaration of competing interest

The authors declare that they have no known competing financial interests or personal relationships that could have appeared to influence the work reported in this paper.

Data availability

Data will be made available on request.

References

Alaña, M., Cutolo, A., Ruiz de Galarreta, S., Van Hooreweder, B., 2021. Influence of relative density on quasi-static and fatigue failure of lattice structures in Ti6Al4V produced by laser powder bed fusion. Sci. Rep. 11, 19314. https://doi.org/10.1038/s41598-021-98631-3.

Ansys® Academic Research Mechanical, 2023. Release 23.2, Help System, Coupled Field Analysis Guide. ANSYS, Inc.

ASTM Standard E9-09, 2019. Test methods of compression testing of metallic materials at room temperature. Annu. Book ASTM (Am. Soc. Test. Mater.) Stand. https://doi.org/10.1520/E0009-19.

Barba, D., Alabort, E., Reed, R.C., 2019. Synthetic bone: design by additive manufacturing. Acta Biomater. 97, 637–656. https://doi.org/10.1016/j.actbio.2019.07.049.

Benedetti, M., du Plessis, A., Ritchie, R.O., Dallago, M., Razavi, N., Berto, F., 2021. Architected cellular materials: a review on their mechanical properties towards fatigue-tolerant design and fabrication. Mater. Sci. Eng. R Rep. 144, 100606. https://doi.org/10.1016/j.mser.2021.100606.

BSI Standards Publication, 2016. Implants for surgery. Partial and total hip joint prostheses. https://doi.org/10.3403/30083053.

Cutolo, A., Van Hooreweder, B., 2022. Fatigue behaviour of diamond based Ti-6Al-4V lattice structures produced by laser powder bed fusion: on the effect of load direction. Mater. Today Commun. 33, 104661. https://doi.org/10.1016/j.mtcomm.2022.104661.

Dias, J.M., da Silva, F.S.C.P., Gasik, M., Miranda, M.G.M., Bartolomeu, F.J.F., 2024. Unveiling additively manufactured cellular structures in hip implants: a comprehensive review. Int. J. Adv. Des. Manuf. Technol. 130, 4073–4122. https://doi.org/10.1007/s00170-023-12769-0.

du Plessis, A., Razavi, N., Benedetti, M., Murchio, S., Leary, M., Watson, M., Bhate, D., Berto, F., 2022. Properties and applications of additively manufactured metallic cellular materials: a review. Prog. Mater. Sci. 125, 100918. https://doi.org/10.1016/j.pmatsci.2021.100918.

Foti, P., Razavi, N., Fatemi, A., Berto, F., 2023. Multiaxial fatigue of additively manufactured metallic components: a review of the failure mechanisms and fatigue life prediction methodologies. Prog. Mater. Sci. 137, 101126. https://doi.org/10.1016/j.pmatsci.2023.101126.

Fu, Z., Körner, C., 2022. Actual state-of-the-art of electron beam powder bed fusion. Eur. J. Mater. 2. https://doi.org/10.1080/26889277.2022.2040342.

Guo, L., Ataollah Naghavi, S., Wang, Z., Nath Varma, S., Han, Z., Yao, Z., Wang, Ling, Wang, Liqiang, Liu, C., 2022. On the design evolution of hip implants: a review. Mater. Des. 216, 110552. https://doi.org/10.1016/j.matdes.2022.110552.

Hanks, B., Berthel, J., Frecker, M., Simpson, T.W., 2020. Mechanical properties of additively manufactured metal lattice structures: data review and design interface. Addit. Manuf. 35, 101301. https://doi.org/10.1016/J.ADDMA.2020.101301.

Hrabe, N.W., Heinl, P., Flinn, B., Körner, C., Bordia, R.K., 2011. Compression-compression fatigue of selective electron beam melted cellular titanium (Ti-6Al-4V). J. Biomed. Mater. Res. B Appl. Biomater. 99B, 313–320. https://doi.org/10.1002/jbm.b.31901.

Huang, Y., Chen, Z.W., Wan, A.R.O., Schmidt, K., Sefont, P., Singamneni, S., 2024. Electron beam powder bed fusion additive manufacturing of Ti6Al4V alloy lattice structures: orientation-dependent compressive strength and fracture behavior. Int. J. Adv. Des. Manuf. Technol. 132, 3299–3311. https://doi.org/10.1007/s00170-024-13539-2.

Jam, A., Pellizzari, M., Emanuelli, L., Valsecchi, G., du Plessis, A., Benedetti, M., 2024. Influence of heat treatment on the mechanical performance of Ti21S octet truss lattice structure fabricated by laser powder bed fusion. Prog. Addit. Manuf. 9, 947–957. https://doi.org/10.1007/s40964-023-00494-9.

Kadkhodapour, J., Montazerian, H., Darabi, A.Ch, Anaraki, A.P., Ahmadi, S.M., Zadpoor, A.A., Schmauder, S., 2015. Failure mechanisms of additively manufactured porous biomaterials: effects of porosity and type of unit cell. J. Mech. Behav. Biomed. Mater. 50, 180–191. https://doi.org/10.1016/j.jmbbm.2015.06.012.

Karami, K., Blok, A., Weber, L., Ahmadi, S.M., Petrov, R., Nikolic, K., Borisov, E.V., Leeflang, S., Ayas, C., Zadpoor, A.A., Mehdipour, M., Reinton, E., Popovich, V.A., 2020. Continuous and pulsed selective laser melting of Ti6Al4V lattice structures: effect of post-processing on microstructural anisotropy and fatigue behaviour. Addit. Manuf. 36, 101433. https://doi.org/10.1016/j.addma.2020.101433.

Khorasani, A., Gibson, I., Veetil, J.K., Ghasemi, A.H., 2020. A review of technological improvements in laser-based powder bed fusion of metal printers. Int. J. Adv. Des. Manuf. Technol. 108, 191–209. https://doi.org/10.1007/s00170-020-05361-3.

Korkmaz, M.E., Gupta, M.K., Robak, G., Moj, K., Krolczyk, G.M., Kuntoğlu, M., 2022. Development of lattice structure with selective laser melting process: a state of the art on properties, future trends and challenges. J. Manuf. Process. 81, 1040–1063. https://doi.org/10.1016/j.jmapro.2022.07.051.

Li, S.J., Murr, L.E., Cheng, X.Y., Zhang, Z.B., Hao, Y.L., Yang, R., Medina, F., Wicker, R. B., 2012. Compression fatigue behavior of Ti–6Al–4V mesh arrays fabricated by electron beam melting. Acta Mater. 60, 793–802. https://doi.org/10.1016/j.actamat.2011.10.051.

Li, S.J., Xu, Q.S., Wang, Z., Hou, W.T., Hao, Y.L., Yang, R., Murr, L.E., 2014. Influence of cell shape on mechanical properties of Ti–6Al–4V meshes fabricated by electron beam melting method. Acta Biomater. 10, 4537–4547. https://doi.org/10.1016/j.actbio.2014.06.010.

Mahmoud, D., Al-Rubaie, K.S., Elbestawi, M.A., 2021. The influence of selective laser melting defects on the fatigue properties of Ti6Al4V porosity graded gyroids for bone implants. Int. J. Mech. Sci. 193, 106180. https://doi.org/10.1016/j.ijmecsci.2020.106180.

Mehboob, H., Tarlochan, F., Mehboob, A., Chang, S.-H., 2018. Finite element modelling and characterization of 3D cellular microstructures for the design of a cementless biomimetic porous hip stem. Mater. Des. 149, 101–112. https://doi.org/10.1016/j.matdes.2018.04.002.

Peng, C., Tran, P., Nguyen-Xuan, H., Ferreira, A.J.M., 2020. Mechanical performance and fatigue life prediction of lattice structures: parametric computational approach. Compos. Struct. 235, 111821. https://doi.org/10.1016/j.compstruct.2019.111821.

Radlof, W., Polley, C., Seitz, H., Sander, M., 2021. Influence of structure-determining parameters on the mechanical properties and damage behavior of electron beam melted lattice structures under quasi-static and fatigue compression loading. Mater. Lett. 289, 129380. https://doi.org/10.1016/j.matlet.2021.129380.

Raghavendra, S., Molinari, A., Cao, A., Gao, C., Berto, F., Zappini, G., Benedetti, M., 2021. Quasi-static compression and compression–compression fatigue behavior of regular and irregular cellular biomaterials. Fatig. Fract. Eng. Mater. Struct. 44, 1178–1194. https://doi.org/10.1111/ffe.13422.

Ren, D., Li, S., Wang, H., Hou, W., Hao, Y., Jin, W., Yang, R., Misra, R.D.K., Murr, L.E., 2019. Fatigue behavior of Ti-6Al-4V cellular structures fabricated by additive manufacturing technique. J. Mater. Sci. Technol. 35, 285–294. https://doi.org/10.1016/j.jmst.2018.09.066.

Schijve, J., 2009. Fatigue of structures and materials. Fatigue of Structures and Materials, second ed. Springer, Dordrecht, Dordrecht. https://doi.org/10.1007/978-1-4020-6808-9.

Sing, S.L., An, J., Yeong, W.Y., Wiria, F.E., 2016. Laser and electron-beam powder-bed additive manufacturing of metallic implants: a review on processes, materials and designs. J. Orthop. Res. 34, 369–385. https://doi.org/10.1002/jor.23075.

Wu, M.-W., Chen, J.-K., Lin, B.-H., Chiang, P.-H., Tsai, M.-K., 2020. Compressive fatigue properties of additive-manufactured Ti-6Al-4V cellular material with different porosities. Mater. Sci. Eng., A 790, 139695. https://doi.org/10.1016/j.msea.2020.139695.

Wu, M.-W., Chen, J.-K., Tsai, M.-K., Wang, P., Cheng, T.-L., Lin, B.-H., Chiang, P.-H., Dhinakar, A., 2022. Uniaxial compression properties and compression fatigue performance of selective laser melted Ti–6Al–4V cellular structure. Met. Mater. Int. 28, 132–144. https://doi.org/10.1007/s12540-021-01021-7.

Wu, Z.Y., Liu, Y.J., Wu, X., Liu, X.C., Wang, J.C., Wang, Q., 2024. Fatigue performance of beta titanium alloy topological porous structures fabricated by laser powder bed fusion. J. Mater. Res. Technol. 29, 4772–4780. https://doi.org/10.1016/j.jmrt.2024.02.190.

Yang, L., Wu, S., Yan, C., Chen, P., Zhang, L., Han, C., Cai, C., Wen, S., Zhou, Y., Shi, Y., 2021. Fatigue properties of Ti-6Al-4V Gyroid graded lattice structures fabricated by laser powder bed fusion with lateral loading. Addit. Manuf. 46, 102214. https://doi.org/10.1016/j.addma.2021.102214.

Yuan, W., Hou, W., Li, S., Hao, Y., Yang, R., Zhang, L.-C., Zhu, Y., 2018. Heat treatment enhancing the compressive fatigue properties of open-cellular Ti-6Al-4V alloy prototypes fabricated by electron beam melting. J. Mater. Sci. Technol. 34, 1127–1131. https://doi.org/10.1016/j.jmst.2017.12.003.

Zhao, S., Li, S.J., Hou, W.T., Hao, Y.L., Yang, R., Misra, R.D.K., 2016. The influence of cell morphology on the compressive fatigue behavior of Ti-6Al-4V meshes fabricated by electron beam melting. J. Mech. Behav. Biomed. Mater. 59, 251–264. https://doi.org/10.1016/j.jmbbm.2016.01.034.

Ziaie, B., Velay, X., Saleem, W., 2024. Advanced porous hip implants: a comprehensive review. Heliyon 10 (2024), e37818. https://doi.org/10.1016/j.heliyon.2024.e37818.